Bandgap engineering via tuning of S and Se content in $Cu_2ZnSn(S, Se)_4$ for improved thermoelectric properties

By
Rabia Ahmed

School of Chemical and Materials Engineering

National University of Sciences and Technology

2023

Bandgap engineering via tuning of S and Se content in Cu₂ZnSn(S, Se)₄ for improved thermoelectric properties

Name: Rabia Ahmed

Reg. No: 00000318991

This thesis is submitted as a partial fulfillment of the requirements.

for the degree of

MS in Nanoscience & Engineering

Supervisor Name: Dr. Muhammad Siyar

School of Chemical and Materials Engineering (SCME)

National University of Sciences and Technology (NUST),

H-12 Islamabad, Pakistan

July, 2023

THESIS ACCEPTANCE CERTIFICATE

Certified that final copy of MS thesis written by Ms **Rabia Ahmed** (Registration No 00000318991), of School of Chemical & Materials Engineering (SCME) has been vetted by undersigned, found complete in all respects as per NUST Statues/Regulations, is free of plagiarism, errors, and mistakes and is accepted as partial fulfillment for award of MS degree. It is further certified that necessary amendments as pointed out by GEC members of the scholar have also been incorporated in the said thesis.

Signature: _____

Name of Supervisor: **Dr Muhammad Siyar**

Date: 06-09-223

Signature (HOD): _____

Date: 07/09/23

Signature (Dean/Principal): _____

Date: 7-9-2023

National University of Sciences & Technology (NUST)

MASTER'S THESIS WORK

Formulation of Guidance and Examination Committee (GEC)

Name: **Rabia Ahmed** NUST Regn No: **318991**

Department: **ME (SCME)** Specialization: **Nanoscience & engineering**

Credit Hour Completed: **24** CGPA: **3.13**

S/No	Code	Title	Core/Elective	CH	Grade
1	MSE-854	Characterization of materials	Core	3	A
2	MSE-856	Nanomaterials and processing	Core	3	B
3	NSE-813	Essentials of nanoscience and engineering	Core	3	B
4	MSE-862	Electronic and magnetic materials	Elective	3	B
5	NSE-812	Environmental nanotechnology	Elective	3	B
6	NSE-941	Nanocomposite materials	Elective	3	B
7	NSE-842	Nanomaterials for energy applications	Elective	3	C+
8	NSE-845	Nanolithography and device fabrication	Elective	3	B+
9	RM-898	Research methodology	Elective	2	Q

Date 28-10-2021

Student's Signature **Rabia Ahmed**

Thesis Committee

1. Name: **Dr. Muhammad Siyar** **(Supervisor)** Signature: _____
    Department: **Materials engineering**

2. Name: **Dr. Muhammad Aftab Akram** Signature: _____
    Department: **Materials engineering**

3. Name: **Dr. Muhammad Irfan** Signature: _____
    Department: **Materials engineering**

Date: _____ Signature of Head of Department: _____ 9/11/21

APPROVAL

Date: _8. 11. 2021_ _____
 Dean/Principal

School of Chemical and Materials Engineering (SCME) Sector H-12, Islamabad

National University of Sciences &Technology (NUST)

MASTER'S THESIS WORK

We hereby recommend that the dissertation prepared under our supervision by Regn No & Name: 00000318991 Rabia Ahmed

Title: **Bandgap engineering via tuning of S and Se content in $Cu_2ZnSn\,(S,\,Se)_4$ for improved thermoelectric properties.**

Presented on: **31 Aug 2023**   at: **1400 hrs in SCME (Seminar Hall)**

Be accepted in partial fulfillment of the requirements for the award of Masters of Science degree in **Nanoscience & Engineering.**
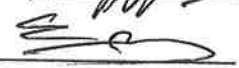
Guidance & Examination Committee Members

Name: **Dr Muhammad Irfan**   Signature:

Name: **Dr Muhammad Aftab Akram**   Signature:

Supervisor's Name: **Dr Muhammad Siyar**   Signature:

Dated: 31-08-2023

Head of Department

Date 31/08/2023

Dean/Principal

Date 4-9-23

School of Chemical &Materials Engineering (SCME)

Dedication

This thesis is dedicated to my beloved Parents & My Respected Teachers without whom I would not be here. Thanks for their endless Guidance and Support

Acknowledgement

Abstract

Thermoelectric materials are in high demand for sustainable energy solutions since they are essential for turning waste heat into usable electrical energy or solid-state refrigeration. Chalcogenides have emerged as promising materials in the field of thermoelectrics, which typically consist of three elements, often including a chalcogen (sulfur, selenium, or tellurium) combined with transition metals or other elements. The unique crystal structure and electronic properties of ternary chalcogenides contribute to their excellent thermoelectric performance. They possess high thermoelectric efficiency due to their ability to simultaneously exhibit low thermal conductivity and high electrical conductivity. In this study quaternary chalcogenides $Cu_2ZnSn(S_x, Se_{1-x})_4$ compounds were synthesized successfully by adopting the mechanochemical alloying (ball milling) method. The synthesis process consists of three main steps: ball milling of elemental precursors, sintering and densification through cold isostatic pressing (CIP). We hereby report the structural characterization and thermoelectric investigations carried out on samples milled at 200 rpm for 3hrs followed by sintering at 500°C. X-ray diffraction (XRD) and EDX were carried out for phase and composition analysis. Thermoelectric properties, such as electrical conductivity (σ), thermal conductivity (K), and Seebeck coefficient (S), were measured over a temperature range of 300–600 K. The maximum thermoelectric figure of merit (ZT) obtained is for $Cu_2ZnSnS_{2.8}Se_{1.2}$.with a value of 0.12 at 600K. These values closely resemble the reported figure of merit for compounds synthesized using solid-state techniques.

Table of Contents

List of Figures

Lists of Table

List of abbreviations

TE   Thermoelectric

CZTS   Copper Zinc Tin Sulfur

CZTSe   Copper Zinc Tin Selenide

TC   Thermocouple

XRD   X-ray diffraction

SEM   Scanning electron microscopy

Uv-Vis   Ultra-violet Visible

σ Electrical Conductivity

K Thermal Conductivity

S   Seebeck

ZT   Figure of Merit

Chapter 1

1 Introduction

The world is currently confronted with several difficulties related to energy production and use. The surge in oil prices has led to a global increase in the demand for oil. Furthermore, there is a rising apprehension regarding the environmental effects of greenhouse gases, especially carbon dioxide. These factors collectively contribute to a growing need for more efficient energy utilization. For instance, various advancements are being made in vehicle engines, gearboxes, and related technologies to enhance fuel efficiency in transportation vehicles. Nonetheless, an important concern remains unaddressed: a considerable amount of the generated energy will still be wasted as unusable heat, either in the vehicle's exhaust or cooling system. In the context of combustion engines, nearly 40% of the fuel energy is discharged as exhaust gas, roughly 30% is dispersed through the engine coolant, and 5% is wasted due to radiation and friction. As a result, only 25% of the energy remains accessible for vehicle mobility and powering accessories [1]

In the present era, fossil fuels play a dominant role as the primary source for generating electrical energy. These fuels, which contain carbon, were formed through geological processes from the remnants of organic matter produced by photosynthesis hundreds of years ago. However, in various industrial processes, a significant amount of energy is lost as waste heat, causing adverse effects on the environment and the overall ecosystem. Consequently, there is a pressing need to explore more efficient and sustainable methods of energy generation to address these challenges effectively [2].

1.1 Thermoelectricity

When subjected to thermal energy, a thermoelectric (TE) material has the capability to convert that thermal energy into electrical energy. The aforementioned phenomenon is facilitated by the diffusion of charge carriers from the region of higher temperature to the region of lower temperature, resulting in the production of an electric current [3]. The presence of a thermal gradient across the thermoelectric (TE) device gives rise to the creation of a potential difference, which subsequently

leads to the generation of electrical voltage. The occurrence being discussed is commonly known as the Seebeck effect.

Conversely, when an electric voltage is applied to a TE device, due to Peltier effect it can utilize this voltage to create a temperature gradient across the material, which can be utilized as a refrigeration system [4].

1.1.1   Seebeck Effect

Thomson Johann Seebeck first proposed the concept of the thermoelectric effect in 1821. When a temperature gradient exists between two linked conductors or semiconductors, a potential difference is created that can induce the movement of electric charge, resulting in the generation of electricity. This is caused by the Seebeck effect, which is triggered by a temperature difference (T) between the two conductors. An electric field is produced as the most charge carriers move away from the hot side toward the cool side [5]. As seen in figure 1.1 this causes charges to build up and spread out [6]. Seebeck coefficient quantifies the proportionality between potential difference and temperature [7]. The following equation can be used to express it mathematically:

$$\mathbf{S} = \frac{\Delta V}{\Delta T}$$

S   = Seebeck coefficient

ΔV = Electric field

ΔT = Temperature gradient
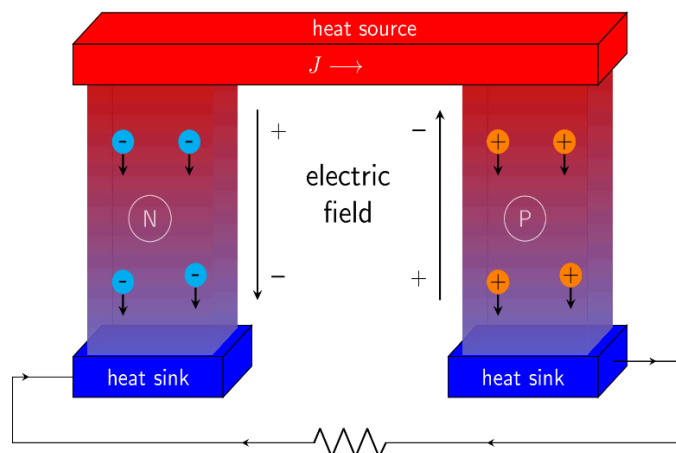
Figure 1.1 Schematic of Seebeck Effect

The Seebeck coefficient for p-type materials is positive, while the Seebeck coefficient for n-type materials is negative [8].

1.1.2 Peltier Effect

The Seebeck effect, first observed by French physicist Jean Charles Athanase in 1834, has an inverse phenomenon known as the Peltier effect. It was observed that when there is a temperature difference (either heating or cooling) across conductors or semiconductors, an electric field is generated between the two sides [9] When this electric field runs through the circuit, it can add or remove heat from the interface between the two materials. [10]. The Peltier effect describes the relationship between heating, cooling, and the electric current as it circulates in the circuit. This effect can be mathematically expressed through the following equation [11]:

$$\Pi = \frac{Q\Pi}{I}$$

Π = Peltier coefficient

I = Absorb heat

QΠ = Applied Heat
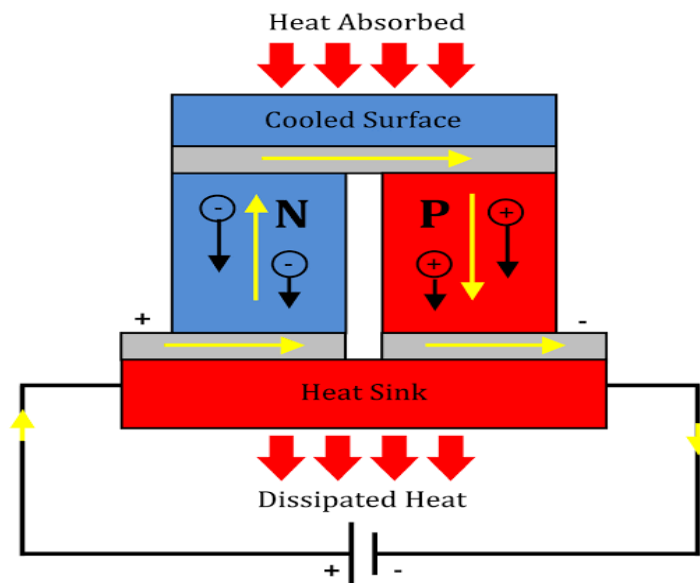
Figure 1.2 Schematic of Peltier effect

1.1.3 Thomson Effect:

In 1854, a significant discovery was made by William Thomson. During his research, he observed that when a particular material is subjected to heat, the heat energy moves from the hotter side to the colder side. Moreover, he noticed that this process also caused the movement of charge carriers within the material, leading to the generation of an electric current. This remarkable phenomenon came to be known as the Thomson effect [12].

The Thomson effect established direct correlation between two other phenomena known as the Peltier effect (which relates to cooling) and the Seebeck effect (which relates to heating). Essentially, the Thomson effect highlights how these three effects are interconnected.

The term "Thomson effect" refers to the creation of a temperature gradient along the length of a material when an electric current is sent through it. The symbol for the Thomson effect is [13];

$$dQ = \beta I dT$$

Where

dQ = rate of heat generation

β = Thomson coefficient

I = Applied current

dT = Temperature difference
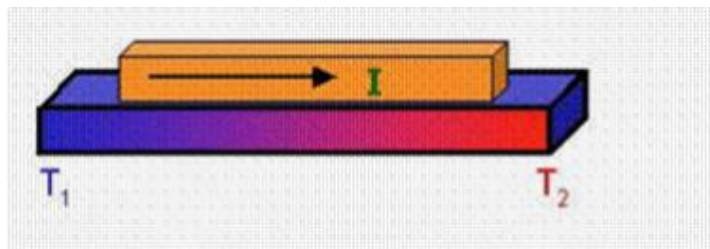
Figure 1.3 Schematic of Thomson effect

1.2 Figure of Merit (ZT)

Loffe, in 1957, proposes the figure of merit (ZT) as a crucial performance criterion for thermoelectric materials. It measures the effectiveness of a substance as a heat-to-electricity converter [14]. It can be represented using the following equations:

4

$$ZT = \frac{S^2}{\rho K} T$$

$$\sigma = \frac{1}{\rho}$$

$$ZT = \frac{S^2 \sigma}{K} T$$

Where:

S = Seebeck co-efficient which is also referred to as thermoelectric power, quantifies the amount of voltage produced per unit temperature difference across the material.

σ = the electrical conductivity of the material, which characterizes its ability to conduct electric current.

T = the absolute temperature at which the thermoelectric process occurs.

κ = the thermal conductivity of the material, which quantifies its ability to conduct heat.

ZT is dimensionless figure of merit, and figure of merit is essentially temperature dependent, as well as generated from temperature dependent material attributes [15]. For the higher value of ZT Seebeck coefficient and electrical conductivity must be high along with low thermal conductivity. The greater the ZT value, the more efficient the thermoelectric material converts heat into electricity or vice versa. Furthermore, thermal conductivity is composed of two components: $k = k_e + k_l$. When the lattice conductivity is poor, the overall thermal conductivity falls. These variables are associated with the carrier concentration and band gap structure [16].

1.3 Electrical conductivity of TE materials

The property of electrical conductivity refers to the intrinsic ability of a material to facilitate the flow of electric current. The electrical conductivity can be expressed as the multiplication of the carrier concentration and the carrier mobility.

$$\sigma = \mu n e$$

The acceptable electrical conductivity value for TE materials is $10^{-5} \mathrm{S}m^{-1}$. That can be achieved through high carrier mobility or high carrier concentration.

1.3.1 Carrier concentration

For enhancing the electrical conductivity of TE materials, carrier concentration plays an important role because electrical conductivity depends on carrier concentration and mobility. For good thermoelectric material, the range of carrier concentration is between 10^{18} to $10^{21} cm^{-3}$ which is a desired value for achieving ideal power factor [17].

1.3.2 Carrier mobility

Carrier mobility is a major variable to improve electrical conductivity. Carrier mobility is an ability that tells us how fast the charge can move among the semiconductors [18].

1.4 Thermal conductivity of TE materials

The capability of a material to conduct heat is called thermal conductivity of that material. The total conductivity depends on two factors that are thermal conductivity of electrons(k_{ele}) and thermal conductivity of lattice(k_{lat}) [19].

$$\mathbf{K} = \boldsymbol{k_{ele}} + \boldsymbol{k_{lat}}$$

To determine the thermal conductivity of electron the Wiedemann- Franz law can be applied.

$$\boldsymbol{k_{ele}} = \mathbf{L}\boldsymbol{\sigma}\mathbf{T}$$

L is Lorentz parameter; and the range of Lorentz parameter is 1.6 to 2.5 WΩk^{-2}. Wiedemann- Franz law states that the thermal conductivity of the electrons increases with the rise in electrical conductivity. That's why suitable TE materials and enhanced carrier concentration is essential to achieve higher ZT [20].

1.5 Thermoelectric (TE) Materials

The global demand for energy resources is rapidly increasing, necessitating the exploration of alternative solutions to meet this growing need. Renewable energy sources have emerged as a vital pathway towards sustainable power generation, mitigating the negative impact on the environment. To enhance our current energy supply, we must focus on harnessing the potential of diverse renewable sources such as solar, wind, biomass, and others. Additionally, an effective method for generating electricity from heat is through the utilization of thermoelectric (TE) materials [21].

Thermoelectric energy (TE) is essentially a direct conversion of waste heat into electrical energy. A thermoelectric material has no moving parts and converts waste heat directly into electrical energy and solid-state cooling. Heat can be produced through the combustion of fossil fuels (e.g., combustion, chemical processes, nuclear decay). Thermoelectric materials have enormous promise for use in mobile devices and distributed heat harvesting applications such as vehicle exhaust heat recovery. The presence of electronic and phononic transport is involved in the thermoelectric phenomenon. The figure of merit (ZT) is used to characterize the efficiency of thermoelectric materials [22].

The thermoelectric effect is observed due to the mobility of charge carriers in semiconductors and metals, which resembles the behavior of gas molecules. These charge carriers possess the ability to transport both electric charge and heat. Heavily doped semiconductors with metal-like transport characteristics are considered to be the most optimal thermoelectric materials due to their ability to effectively control the movement of electrons and phonons. [23]. Chalcopyrite-type semiconductors are attractive materials for multiple applications due to their unique electronic and optical properties, making them suitable for photovoltaics, light-emitting diodes, nonlinear optics, and thermoelectric devices [24-27]. Chalcogenide compounds, including ternary and quaternary ones, can be designed by combining elements from various groups. These tetrahedrally coordinated semiconductors compounds such as stannite and famatinite have been recommended [28, 29].

Cu-based quaternary chalcogenide compounds are attracting significant attention due to their potential similarities with ternary photovoltaic absorbers from I-III-VI$_2$ compounds. These compounds belong to the I$_2$-II-IV-VI$_4$ family. Cu$_2$ZnSnS$_4$ (CZTS) and Cu$_2$ZnSnSe$_4$ (CZTSe) are quaternary semiconductors that have gained attention as potential absorber layers for thin film solar cells [30]. The aforementioned materials possess high absorption coefficients above 10^4 cm^{-1}, exhibit a desirable band gap values and are abundantly accessible in the earth's crust. Consequently, they are highly appealing for use in solar cell applications. CZTSSe, which are solid solutions of Cu2ZnSnS4 (CZTS) and Cu2ZnSnSe4 (CZTSe), exhibit promise as absorber layers in thin-film solar cells. The crucial criterion for achieving high efficiency in thin film solar cells is the band gap of the absorber layer [31]. Many researchers have discovered that varying the amount of sulfur and selenium in the material can affect the band gap (E_g). However, there is still some disagreement

about how exactly the band gap (E_g) changes with the composition. So, these quaternary semiconductors compounds exhibit desirable band gap and absorption coefficient characteristics. As CZTS has band gap of approximately 1.5 eV, while CZTSe has a band gap of approximately 1 eV. The current best semiconductors compounds e.g. Bi_2Te_3, PbTe and SiGe work well at different temperatures, from near room temperature to high temperatures, and they are very efficient. One problem is that at high temperatures, the performance of the material performance starts to decrease because of bipolar effect. PbTe, for example, performs well at medium temperatures, but at 900 K (high temp) its thermal conductivity becomes too high and hinders its performance because PbTe has a very narrow band gap value of 0.3 eV, which causes problem known as bipolar effect. To address this issue, researchers need materials featuring wider band gaps, which can mitigate the bipolar effect and lead to improved thermoelectric performance. Utilizing materials with wide band gaps proves valuable in reducing the bipolar effect and enhancing thermoelectric performance. According to Mahan et al. materials with a band gap value (E_g) of 1 to 1.5 eV are being studied to reduce the bipolar effect. Examples of such materials include kesterites, tetrahedrites, and clatherites [30].

The Kesterite CZT(S, Se) system of compounds is widely utilized as a photovoltaic absorber. In recent times, numerous research groups worldwide have been exploring these compounds as promising contenders for thermoelectric power generation. These compounds possess a tetragonal structure with either the space group I_4 (Kesterite) or I_42m (Stannite) [30]. Cu2ZnSnS4 (CZTS) is well recognized as a prominent compound that has garnered considerable interest in the field of thin-film solar cells. This can be attributed to its composition, which consists of numerous elements found on Earth and is free of hazardous properties. These compounds exhibit intriguing optoelectronic properties, making them very desirable for utilization in heat energy conversion and diverse electronic devices..

1.6 Application of TE Materials:

Advancements in materials have led to the development of more efficient options, expanding potential of thermoelectric energy for generators and coolers. Numerous studies have focused on discovering highly efficient TE materials, particularly nanostructured ones [32]. One significant application of thermoelectric technology is

power generation through thermoelectric generators (TEGs), which function as power harvesters. TEGs can convert waste heat directly into electricity [33]-[34].

In the automotive industry, thermoelectric devices offer unique features divided into two categories: the Peltier effect and the Seebeck effect. The Peltier effect and the Seebeck effect are two phenomena that are commonly studied in the field of thermoelectricity. The Peltier effect is concerned with the conversion of electrical energy into cooling, whereas the Seebeck effect involves the conversion of waste heat into usable electrical energy. These approaches not only exhibit high efficiency but are also environmentally friendly, as they pose no hazards [35].

Wearable technology is one area where the use of human body heat to run tiny sensors and health monitoring system. As wearable devices become more common in our lives, there is an increasing demand for efficient and dependable power sources to keep them running. The heat produced by the body can be transformed into electrical energy to power these gadgets by incorporating thermoelectric modules into wearable devices. This improves not just their usability and convenience, but also lessens their dependency on standard batteries and increases their lifetime [36].

Furthermore, portable electronics can use heat from the human body to improve their functionality and usability. Consider a smartphone that charges its battery or powers its operations by using the heat from your hand. These gadgets can become more self-sustaining by combining thermoelectric materials and designs, lowering dependency on traditional charging methods, and improving energy efficiency.

While the idea of harnessing the heat of the human body for TE applications is still in its early phases, continued research and development shows promise for broadening its practical applicability. We can unlock the full potential of using the human body as a reliable and sustainable heat source for various applications by exploring new materials, optimizing device designs, and improving the efficiency of thermoelectric modules, paving the way for a greener and more energy-efficient future [37].

1.7 Advantages of TE materials:

Thermoelectric materials have become a significant resource for renewable energy applications, offering numerous advantages. One significant advantage is the solid-

state nature of thermoelectric (TE) devices, which eliminates the requirement for moving parts. This property improves the dependability and efficiency of TE systems. Unlike typical cooling systems, which rely on compressors, TE devices work without such components, resulting in faster response times. Furthermore, TE devices make less noise than compressor-based technologies, making them more appealing in noise-sensitive areas [38].

In addition to these benefits, TE materials provide several others. Because there are no moving parts, they have a high durability and are less vulnerable to mechanical wear and tear. The absence of mechanical components reduces the maintenance requirements and extends the lifespan of TE devices, which contributes to their overall cost-effectiveness [38].

Solid state TE devices can also be arranged in any orientation. The ability to arrange TE devices in any orientation allows for efficient heat transfer and the best use of available space [39].

1.8   Thermoelectric module:

The thermoelectric module is made of n-type and p-type materials. When heat is applied, electrons flow to one side and holes to the other. TE materials with a majority of charge carriers in the n-type and where electrons are dominant in nature are referred to as n-type TE materials, whereas those with a majority of charge carriers in the p-type or where holes are dominant are referred to as p-type TE materials [40].
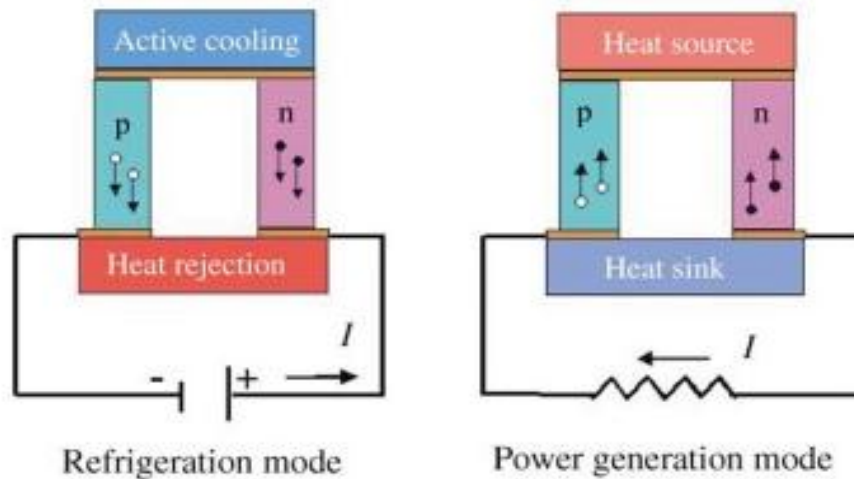
Figure 1.4 TE module of n-type and p-type TE materials

1.9 Choice of TE materials:

Figure 1.5 illustrates the fluctuation in the value of the figure of merit from 1960 to 2016. TE materials are divided into three parts the ZT value is less than 1 and the efficiency of power conversion is 4-5%. Between 2004 and 2010, the ZT value was improved from 1 to 1.7 and the efficiency from 11% to 15% and in third part the high-performance TE materials showed a ZT value of 1.8 and an efficiency of 15% to 20%. It also shows a shift toward chalcogenides. According to the research and graph the SnSe shows good physical and chemical properties [41].
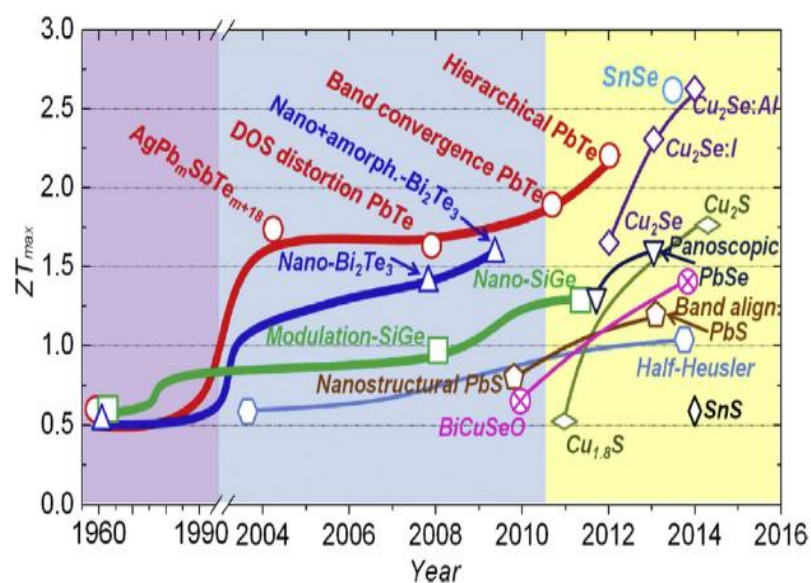
Figure 1.5 figure of merit value variation between 1960 and 2016

Figure 1.6 shows the Sn and Se are both abundant as well as low-cost materials as compared to other options. That's why we are using chalcogenides in our research work. Selenides are high performance thermoelectric materials and highly efficient. Compared to the other sulfides and oxides SnSe is cheaper and environmentally friendly as well [41].
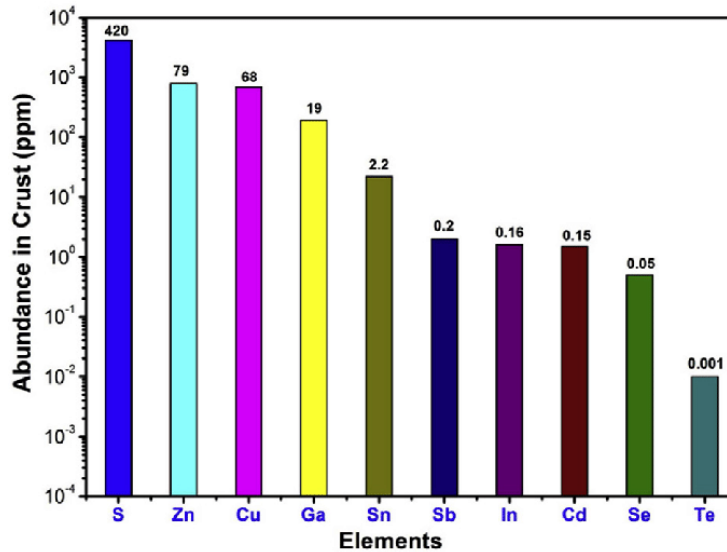
Figure 1.6 Abundance of different TE materials

1.10 Material Selection Criteria:

To have an improved set of TE properties, a material must have a higher ZT value. The material selection criteria are depicted in Figure 1.7. The graph illustrates that semiconductor materials exhibit moderate values for the essential parameters of ZT, which include electrical conductivity, Seebeck coefficient, and thermal conductivity. This characteristic makes semiconductors the most suitable class of materials for thermoelectric research.

For efficient thermoelectric materials, low heat conductivity is required. Thermal conductivity is divided into two parts: k_l, which depends on the crystal lattice vibration, and k_e, which is generated from the electronic portion or charge carriers. It is critical for a TE material to have a bandgap value of less than 1eV in order to attain a higher carrier concentration while maintaining acceptable carrier mobility [42].

Fig shows that three classes of materials: insulators, semiconductor and metals. Each class has distinct thermoelectric properties that determine their suitability for thermoelectric applications. Insulators have low thermoelectric efficiency because of their low ZT value, poor electrical conductivity σ, and high Seebeck coefficient. So, it limits the overall performance of thermoelectric devices. As a result, insulators are generally not considered efficient for thermoelectric applications.

On the other hand, metals have a low Seebeck coefficient but strong electrical conductivity σ and thermal conductivity k. This combination leads to a low ZT value, also making metals less suitable for thermoelectric properties.

However, semiconductors present a potential approach for thermoelectric applications. They have low electrical conductivity, a high Seebeck coefficient, and a low thermal conductivity. High ZT values can be achieved because of this special combination. Due to their ability to produce a considerable voltage over a temperature gradient, semiconductors are effectively able to transform temperature differences into useful electrical energy [43].
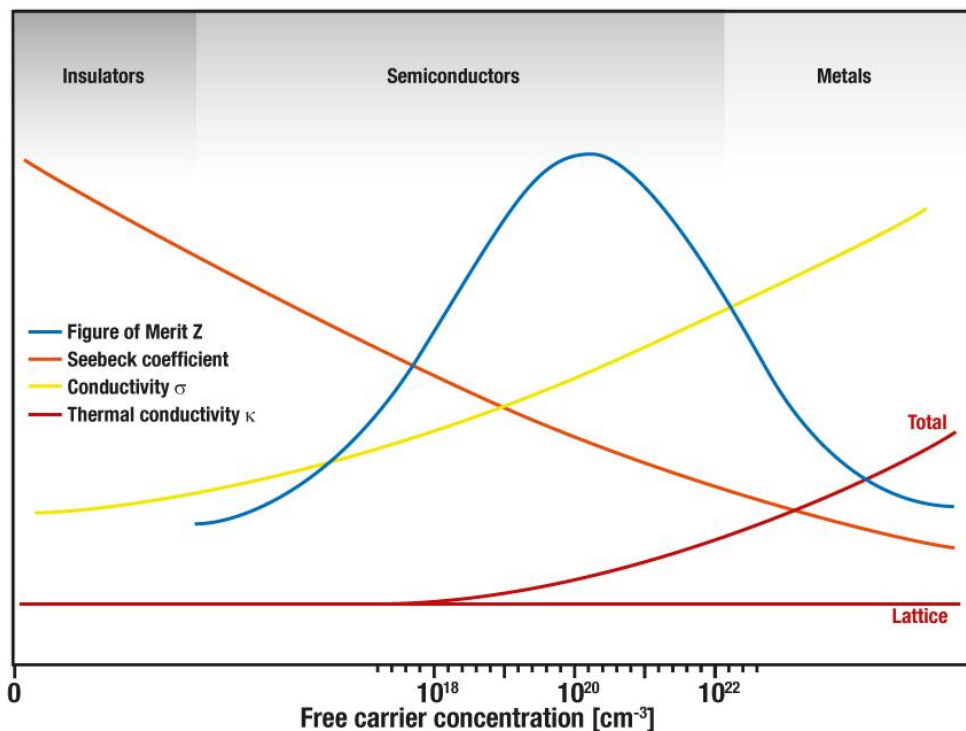
Figure 1.7 Dependence of ZT on carrier concentrations

Chapter 2

2 Literature Review

In this research our major focus is how to improve thermoelectric properties of $Cu_2ZnSn(S,Se)_4$. $CZT(S,Se)_4$, which exhibits amazing promise for efficient and affordable energy conversion, has recently become a fascinating material in the field of thermoelectric.

2.1 Metal chalcogenides

Metal chalcogenides are chemical compounds that contain at least one chalcogen anion and at least one or more electropositive elements. The elements included in group VIA are referred to as chalcogens [44]. Selenides, tellurides, and sulfides are frequently referred to as metal chalcogenides. Metal chalcogenides exist with different composition like binary, ternary and quaternary etc. along with different structures as well [45].

Materials made of two or more elements from the periodic table are known as compound semiconductors. These elements come together to create a crystal structure that possesses special electrical and optoelectronic properties.

Two elements, such as silicon carbide (SiC) or gallium arsenide (GaAs), make up binary semiconductors. Three elements are required for ternary semiconductors like copper indium gallium selenide (CIGS) or gallium indium arsenide (GaInAs). Quaternary semiconductors, as the name suggests, have four elements and include compounds like InGaAsP or Cu2ZnSnS4.

These compound semiconductors have an advantage over elemental semiconductors like silicon (Si) because they can engineer and fine-tune their electrical characteristics by changing the elemental composition. Due to their versatility, these materials are useful for a variety of electrical and optoelectronic applications [46]. **Fig 2.1** shows the elemental composition of binary, ternary and quaternary semiconductors.

Elemental	Binary	Ternary	Quaternary
	BN	$ZnSiN_2$	$LiGaGe_2N_4$
C	$GaAs$	$ZnGeN_2$	$LiAlGe_2N_4$
Si	$AlAs$	$ZnSnN_2$	$CuAlGe_2As_4$
Ge	InN	$ZnGeAs_2$	$NaAlSi_2P_4$
	GaN	$CdSnAs_2$	$AgInSn_2As_4$
IV	III-V	II-IV-V_2	I-III-IV_2-V_4
	II-VI	I-III-VI_2	I_2-II-IV-VI_4
	ZnS	$CuInS_2$	Cu_2ZnSnS_4
	CdS	$CuInSe_2$	Cu_2ZnSnS_4
	$ZnSe$	$CuGaSe_2$	$Cu_2ZnGeSe_4$
	$CdTe$	$AgGaSe_2$	$Ag_2ZnSnSe_4$
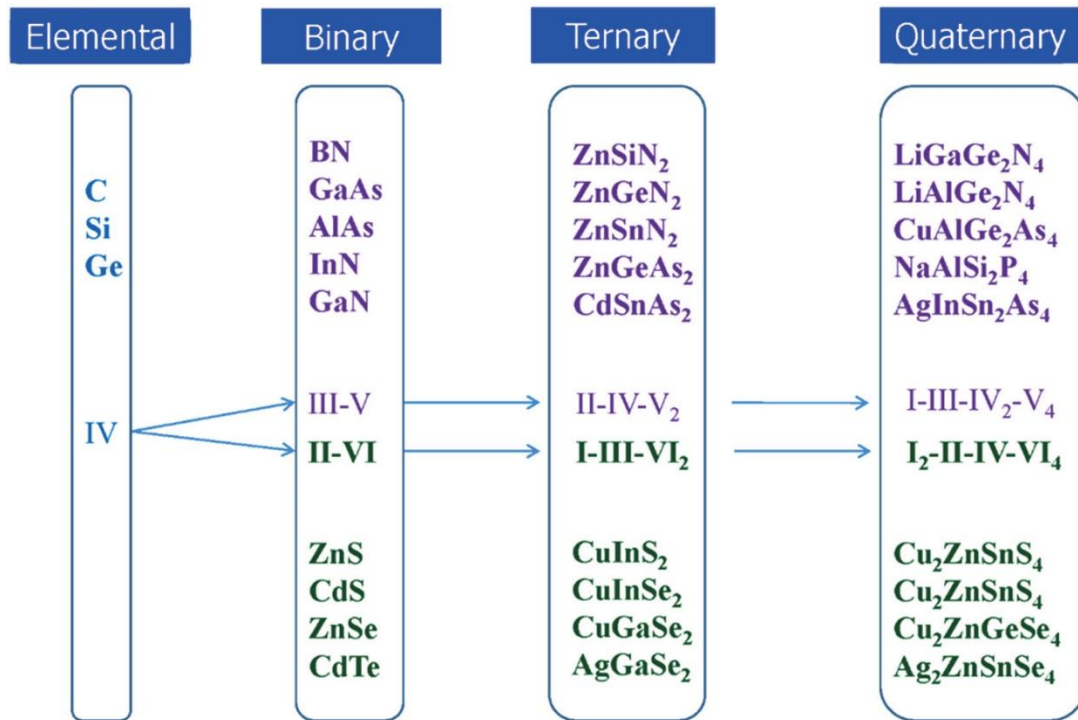
Figure 2.1 Schematic diagram of binary, ternary and quaternary semiconductors

2.2   Structure of CZTS

CZTS is a semiconductor compound with a kesterite structure. Its composition basically consists of a blend of Cu_2FeSnS_4 and Cu2ZnSnS4. Kesterite typically has a metallic luster and a greenish black in colour. CZTS is classified within the category of metal chalcogenides. Due to its low thermal conductivity and high electrical conductivity. CZTS are included among the efficient thermoelectric materials. The compound semiconductor Cu2ZnSnS4 (CZTS) is classified under the crystal structure of Group I2-II-IV-VI4. CZTS is obtained by the modification of CuInS2 by replacing the indium (In) atoms, belonging to Group III, with zinc (Zn) atoms from Group II and tin (Sn) atoms from Group IV. Copper Zinc Tin Sulfide (CZTS) has a

tetragonal crystal structure, which classified under the spacegroup I_4 (known as Kesterite) or I_42m (known as Stannite).[46].

Atoms of Cu_2ZnSnS_4 (CZTS) crystal structure are joined together by chemical bonds. It has an atomic arrangement in three dimensions and a bulk crystal structure. The atoms of copper (Cu), zinc (Zn), tin (Sn), and sulfur (S) are related by covalent bonds inside the lattice structure.
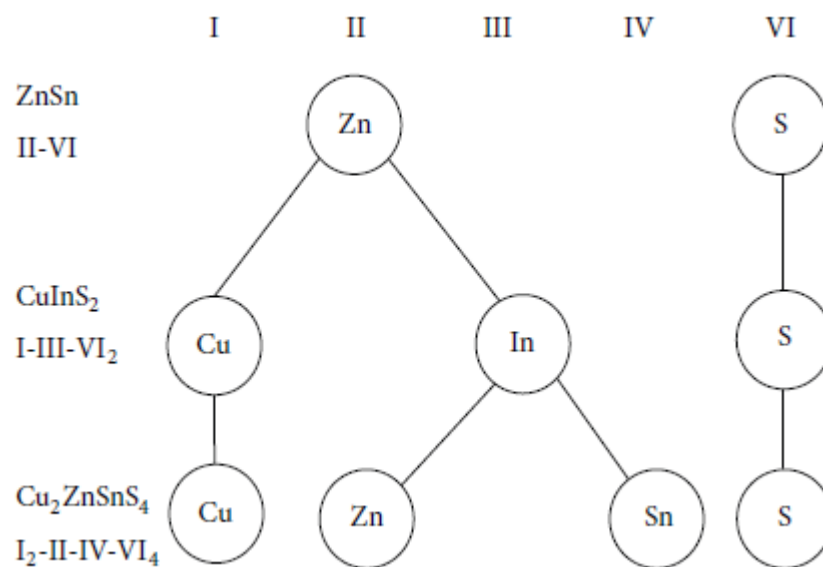
Figure 2.2 The evolutionary graph of CZTS

Cu_2ZnSnS_4 can be classified into two distinct forms, namely kesterite and stannite, based on the varying locations of Cu and Zn., as depicted in Figure 2.3. It can be observed in fig 2.3 that stannite develops from (001) oriented CuAu and kesterite from (201) orientated Chalcopyrite [46].
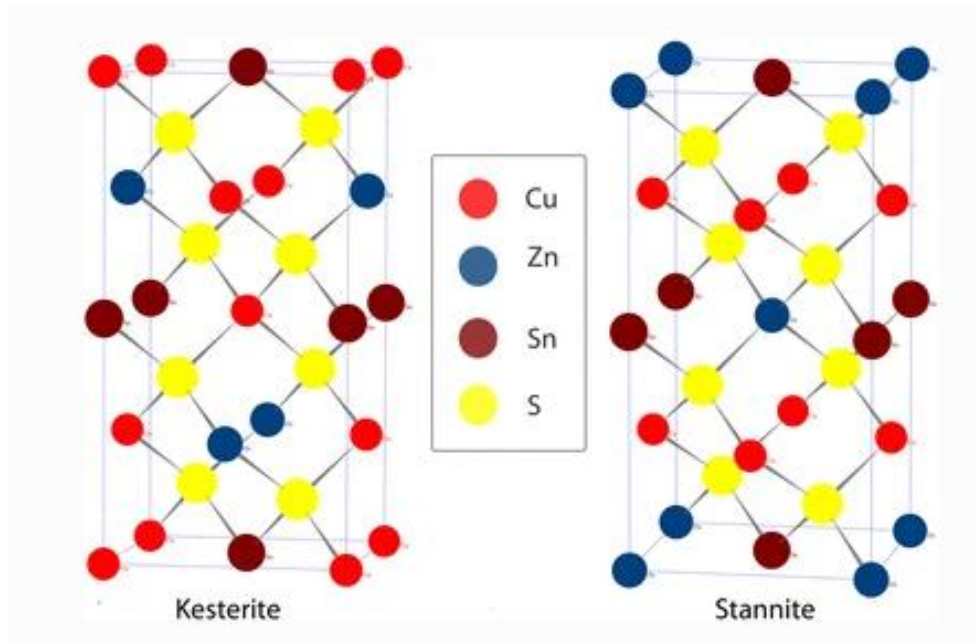
Figure 2.3 Structure of kesterite and stannite for CZTS

Band gap values for Cu2ZnSnS4 (CZTS) typically lie between 1.0 and 1.5 (eV). Cu_2ZnSnS_4 (CZTS) is a promising candidate for absorber materials in thin-film solar cells due to its band gap range of 1.0 to 1.5 eV. Due to its considerable band gap range Copper zinc tin sulfide (CZTS) is a highly appealing option for thin-film solar cell applications, enabling efficient light absorption and holding potential for sustainable energy generation. [30].

2.3 Structure of CZTSSe

CZTSSe also belongs to the family of metal chalcogenides. It is a semiconductor compound with a kesterite structure. It consist of layers of copper (Cu), zinc (Zn), tin (Sn), and chalcogen (S, Se) atoms. The main distinction is whether selenium (Se) or sulphur (S) is present in the crystal structure. CZTS is composed of sulfur atom whereas selenium and sulfur atoms combine to form CZTSSe. This substitution of chalcogen elements affects the thermoelectric properties of the materials. Due to the introduction of selenium, CZTSSe exhibits a tunable bandgap and improved thermoelectric properties. CZTSSe has a tetragonal crystal structure. The band gap of CZTSSe typically ranges from 1.0 to 1.5 [46].

2.4   Reports on Synthesis of CZT(S,Se)

Feng Gao successfully synthesizes CZTSSe solid solution, and its films were made using the printing and high-pressure sintering (PHS) method. The solution was synthesized at 550^oC in inert (N_2) environment. The lattice parameters, denoted as a and c, exhibit a consistent reduction as the concentration of S increases. Based on the scanning electron microscopy (SEM) pictures, it can be shown that the CZTSSe films exhibit a high level of density, while the grain size of these films measures less than 1 m. The band gap value (Eg) of the solid solution CZTSSe exhibits a consistent increase, ranging from 1.05 eV for CZTSe (x=0:0) to 1.51 eV for CZTS (x=1.0) [47].

Kunal J. Tiwari successfully synthesized CZTSSe quaternary chalcogenides by using mechanochemical ball milling technique. The medium used for the wet milling procedure was toluene. The first sample was rotated at 300 revolutions per minute (rpm) for 48 hours, while the second sample was rotated at 500 rpm for 6 hours. The presence of the CZTSe kesterite phase, as well as secondary phases such as ZnSe, has been verified by the utilization of X-ray diffraction (XRD) and energy-dispersive X-ray spectroscopy (EDX). To further understand the thermoelectric behaviour, electrical resistivity and Seebeck coefficient measurements were made on the hot-pressed samples between 340 and 670 K temperature range. Based on the resistivity measurements, it can be inferred that the samples exhibited metallic properties. Additionally, the positive values of the Seebeck coefficient indicated that the samples were characterized as p-type conductors. The thermoelectric figure of merit (ZT) value is 0.15 for the sample that was milled at 300 rpm and 0.16 for the sample that was milled at 500 rpm at temperature 630K. These values are very similar to the reported figure of merit for compounds synthesized by using solid-state techniques [48].

Jun He sing the solid state reaction approach, synthesized the CZTSSe solid solutions. The lattice parameters a and c of CZTSSe decrease linearly with increasing sulfur concentration. Absorption spectra show that the band gaps of CZTSSe solid solutions increase roughly linearly with increasing S concentration. The mass effect and the various bond-stretching force constants lead the peaks of CZTSe and CZTS

to move to a higher frequency in Raman spectra when the S content increases. Additionally, a band gap value of 0.08 eV was discovered. [49].

Chinnaiyah Sripan conducted the synthesis of CZTSSe alloys using the thermal melt technique. The researchers also examined the influence of an excessive quantity of selenium on the synthesis of CZTSSe alloys. The crystallographic structure and phase were verified through the utilization of XRD and Raman spectroscopy techniques. The Raman spectroscopy analysis reveals a transition in phase occurring within the range of 327 cm-1 to 338 cm-1, corresponding to a selenium excess of 5%. The CZTSSe alloys exhibited a measured band gap ranging from roughly 1.43 eV to 1.44 eV. [50].

Vu Minh Han Cao synthesized CZTS NPs by Hot injection technique. The deposition of CZTS ink onto the substrate was achieved using a screen-printing process. The kesterite crystal structure of the photo-sintered copper zinc tin sulfide (CZTS) thin film was determined through the utilization of X-ray diffraction (XRD) analysis. Following the treatment, it was seen that the morphology and crystallization exhibited improvements, as evidenced by the analysis of the Raman spectrum and the examination of the FE-SEM images. The photo-sintered CZTS thin film solar cell device demonstrated an overall cell efficiency of 1.01% when operating at an energy density of 2.96 J/cm2. Despite the fact that the device's efficiency is lower than it was with the old thermal sintering method, it was successfully built. [51].

Bhagyashree Pani uses a doctor blade to prepare thin film absorber layers with a tetragonal kesterite structure. With this method, precursors that have been ball milled can be used to create kesterite films. The chalcogen elements sulfur (S) and selenium (Se) are of significant importance in the mechanisms involved in phase formation and grain development. The use of precursors produced through solid state reaction and film deposition via a non-vacuum blade coating technique, afterwards subjected to annealing, is widely considered as a highly advantageous strategy for the efficient manufacturing of solar cell absorbers on a large scale. A bandgap value (Eg) of 1.38 eV was measured [52].

Umme farva and Chan Park use a simple solid state reaction method to prepare Cu2ZnSnSe4 (CZTSe) materials. SEM and transmission electron microscopy (TEM) results indicate that the particles exhibit a spherical shape and possess a non-uniform size distribution, ranging from approximately 70 to 20 nanometers, subsequent to heat treatment at a temperature of 500 degrees Celsius. X-ray diffraction (XRD) confirms the (CZTSe) stannite phase. They suggested that by controlling the annealing temperature and time, which is a critical factor, it is possible to change the shape and size of the nanostructures [53].

M. N. Solovan obtained $Cu_2ZnSn(S,Se)_4$ films by using a direct current magnetron sputtering. X-ray diffraction (XRD) confirms the $Cu_2ZnSn(S,Se)_4$ has a kesterite phase. Its crystallite size lies between 51–73 nm [54].

Meenakshi Sahu prepared Cu2ZnSnSe4 (CZTSe) nanoparticles with a kesterite structure via wet ball milling. The prepared NP's were used for ink production. In order to increase ink stability, reduce agglomeration and improve adhesion, surfactants and binders were used. The films were deposited via the spin coating technique and subsequently annealed at various temperatures in the presence of selenium within an inert atmosphere. XRD and Raman spectroscopy tells the formation of CZTSe structure with single phase. The thin films underwent examination of their surface morphology and chemical content both before to and during annealing. This examination was conducted using FE-SEM for surface morphology analysis and EDX for chemical composition analysis. The CZTSe thin films exhibited an optical bandgap ranging from 0.82 eV to 1.02 eV, suggesting their classification as p-type materials. [55].

Qijie Guo uses hot injection method to fabricate the CZTS nanoparticles of 16nm in 2009. They also fabricated the CZTS nano thin films by drop casting method. Through this method they obtained a conversion efficiency of 0.8%. The produced nano crystals, with dimensions ranging from 15 to 25 nm, were examined using transmission electron microscopy (TEM). Additionally, a band gap value of 1.5 eV was determined for CZTS nanocrystals. The powder X-ray diffraction (PXRD) method is employed to analyze CZTS nanocrystals, revealing the presence of the kesterite phase in the CZTS material [56].

S.S. Fouad used the inexpensive chemical bath deposition (CBD) technique to produce high-quality CZTS thin films of thicknesses 240 nm – 418 nm on a cleaned glass substrate for 3, 5, and 8 hours. CZTS thin films with a kieserite phase were found via XRD analysis. There was a clear change in the energy gap from 1.54 to 1.48 eV in the studied films. According to EDX study, the prepared film compositions have good stoichiometry. A thorough investigation has been done to investigate how the optical and opto-electrical characteristics of CZTS change with the amount of time they are deposited. An observable correlation has been noted between the lengthening of the deposition time and a significant rise in the nonlinear parameters. This finding may clarify the possibility of using CZTS in nonlinear devices. The DC conductivity of CZTS thin films and its temperature dependence has been addressed. Activation energy values have reduced with increasing film thickness, indicating more consistency in the films' composition. [57].

Yongkwan Dong synthesized quaternary $Cu_{2+x}Zn_{1-x}SnSe_4$, (x = 0, 0.15, 0.2) stannites by melting, annealing, and hot pressing in order to study their high temperature thermoelectric properties. Rietveld refinement and elemental analysis, both techniques were combined to confirm the composition of each specimen. The thermoelectric properties of the material under investigation were evaluated and compared to those of Cu2ZnSnSe4 within the temperature range of 300 K to 800 K. The thermal conductivity of the material system decreases significantly as the concentration of Cu increases at elevated temperatures, primarily as a result of the crystal structure. The specimen with the highest copper concentration, $Cu_{2.2}Zn_{0.8}SnSe_4$, had a maximum ZT value of 0.86 at a temperature of 800 K [58].

Deepak Goyal used a direct dry milling technique to fabricate bulk material of single-phase Cu2ZnSnSe4 (CZTSe) within a controlled inert atmosphere.The primary objective of this study is to enhance the synthesis conditions for single phase CZTSe through the utilization of a dry ball milling technique, hence eliminating the necessity for additional post-processing methods like as annealing, sintering, hot pressing, and so forth. Following the completion of the phase transition. Thin films of Copper Zinc Tin Selenide (CZTSe) absorber were produced using the electron beam evaporation technique. The thin films underwent a manufacturing process at a temperature of 100 °C, followed by vacuum annealing at 480 °C. Subsequently,

several characterisation techniques were employed to analyze the films, including X-ray diffraction (XRD), Raman spectroscopy, optical absorption analysis, and photoresponse testing. The objective of these evaluations was to evaluate the appropriateness of the thin films for utilization in photovoltaic applications. [59].

Pāvels Narica used a vacuum evaporation technique to create CZTSe films on a glass substrate. The time of evaporation was 10 min. Samples were annealed at temperatures ranging from 150°C to 400°C with a step of 50°C in order to obtain the compound $Cu_2ZnSnSe_4$. In this research the main focus was on morphology of CZTSe films at different annealing temperatures. Minimal temperature of transition from amorphous phase to the crystalline phase was determined [60].

Dao Anh Tuan using the spin-coating technique to prepare CZTS structure and then the film is transformed into the CZTSSe utilizing a graphite box and tube furnace during the selenization process. The primary objective of this study is to examine the structural, optical, electrical characteristics, and composition of CZTSSe. This investigation involves maintaining a constant annealing temperature while varying the mass of Se powder. By substituting element S with Se, a morphology characterized by high density packing and a significant increase in grain size has been successfully attained. They achieved p-type CZTSSe films with band gap energy value of 1.27 eV, 1.7×10^{19}cm^{-3} hole concentration and 0.57 Ω.cm resistivity [61].

Arslan Ashfaq utilized the sol-gel process to deposit CZTS thin films onto an ITO substrate. The CZTS thin films underwent sulfurization in a tube furnace, with different durations of time (20, 40, 60, and 80 minutes) at a constant temperature of 500 °C. The findings of the study indicated that a decrease in sulfurization time duration from 80 to 20 minutes resulted in an increase in the Seebeck coefficient value from 67 to 753 V/°C. The positive Seebeck coefficient values observed in the sample indicate that holes are the dominant charge carriers in the growth of CZTS. The presence of secondary phases in the samples that were produced was detected by various characterization techniques, one of which was the observation of a rise in the Seebeck coefficient as the sulfurization time decreased. The Raman spectroscopy analysis revealed that the CZTS/ITO sample, which underwent a sulfurization

process for a duration of 80 minutes, exhibited a reduced presence of secondary phases. X-ray diffraction (XRD) analysis additionally verifies that the CZTS/ITO sample exhibits significantly inferior crystal quality in comparison to samples containing secondary phases. [62].

Sarita Devi Sharma prepared (CZTS) sphere like particles by using microwave synthesis. The utilization of X-ray diffraction (XRD) analysis provides confirmation about the establishment of a tetragonal crystal structure in the compound known as CZTS. The formation of single phase of CZTS with characteristics peak at 334.1 cm^{-1} is confirmed by Raman spectroscopy. The scanning electron microscopy (SEM) analysis reveals that the CZTS particles have a spherical morphology, characterized by a consistent size range of around 250-350 nm. At a temperature of 623K, the hot-pressed CZTS system demonstrates a PF of 21 W/mK^2 and a figure of merit (ZT) of 0.024 [63].

Cu2.1Zn0.9SnSe4 alloys were created by Fahad Mehmood by the process of high-temperature melting. The main aim of this study is to investigate the influence of annealing temperature on the microstructural features and thermoelectric capabilities of Cu2.1Zn0.9SnSe4 alloys. The compounds undergo annealing at four discrete temperatures, specifically 600 °C, 650 °C, 700 °C, and 725 °C. The application of X-ray diffraction (XRD) analysis offers verification of the existence of the Cu2ZnSnSe4 phase, as well as the detection of some other phases. The annealing temperature has a significant impact on the microstructure of Cu2.1Zn0.9SnSe4. The average grain size exhibits an increase, ranging from 7.3 to 12.1 micrometers, as the annealing temperature is raised from 600°C to 725°C. The augmentation of the annealing temperature from 600 to 700 °C resulted in an elevation in thermal conductivity and a concomitant reduction in the figure of merit. The power factor exhibits a rise with the augmentation of grain size. When the grain size was increased from 7.3 to 11.4 μ m, the dimensionless figure of merit was found to slightly drop, but when the grain size was increased to 12.1μm, it significantly increased. The sample exhibiting the highest power factor and possessing moderate thermal conductivity, when compared to the other samples, finally had the highest ZT value of 0.1, as determined at a temperature of 673 K [64].

Sonam Tripathi successfully deposited a thin film of CZTSSe using the thermal evaporation approach after being successfully synthesized in powder form using the melt quench method. The creation of the CZTSSe (kesterite) structure with a tetragonal unit cell is confirmed by XRD measurements. Additionally, data from Raman, SEM, and FTIR confirm the findings and rule out the presence of any other secondary phases or undesirable contaminants. Most notably, the material is best suited for the solar cell application since the optical bandgap E_g was calculated experimentally to be 1.42 eV and the absorption co-efficient was $10^4 \, cm^{-1}$ [65].

2.5 Objective of our research

The objective of this research is to investigate and analyze thermoelectric properties of $Cu_2ZnSn(S,Se)_4$ as a potential candidate for efficient thermoelectric energy conversion. The study aims to understand the effects of varying compositional parameters, such as sulfur content, on the material's thermoelectric performance, specifically focusing on the Seebeck coefficient, electrical conductivity, and thermal conductivity. Additionally, the research will explore the influence of band gap engineering on the thermoelectric efficiency of CZTSSe. Through experimental characterization and theoretical modeling, the research seeks to identify the optimal conditions that result in enhanced thermoelectric efficiency. The results of this study have the potential to expand our understanding of thermoelectric materials and shed light on how CZTSSe can be used in sustainable energy harvesting and waste heat recovery systems.

Chapter 3

3   Experimental work

3.1   Materials

Elemental powders of copper (Cu), zinc (Zn), tin (Sn), sulfur (S), and selenium (Se) were purchased from Sigma-Aldrich and put to use directly in the absence of any further processing.

3.2   Synthesis of $Cu_2ZnSn(S,Se)_4$

The $Cu_2ZnSn(S_x, Se_{x-1})_4$ sample was prepared through a synthesis process involving the reaction of Cu, Zn, Sn, S, and Se powders in stoichiometric proportions. Initially, Cu, Zn, Sn, S, and Se were mixed according to different compositions as mentioned in Table 1 and placed inside a 150 ml steel jar. Steel balls with varying diameters (3mm, 5mm, and 10mm) were added to the jar along with the powder. The ball-to-

powder ratio was maintained at 10:1, with 10 gm of powder and 200 gm of balls. Subsequently, the steel jar was transferred to a glove box and purged with argon gas. Once the argon gas purging was completed, the steel jar's sealing lid was tightly closed, creating an argon-filled atmosphere to protect the powder. Next, the sealed steel jar was placed inside a Pulverisette 5 planetary ball mill and subjected to mechanical alloying for 3 hours at a speed of 200rpm. This milling process aimed to obtain $Cu_2ZnSn(S_x, Se_{x-1})_4$ powder. After completing the mechanical alloying, the steel jar was opened within the glove box, maintaining an inert atmosphere to prevent oxidation. Figure 3.1 provides a visual representation of the synthesis process used to form $Cu_2ZnSn(S_x, Se_{x-1})_4$.
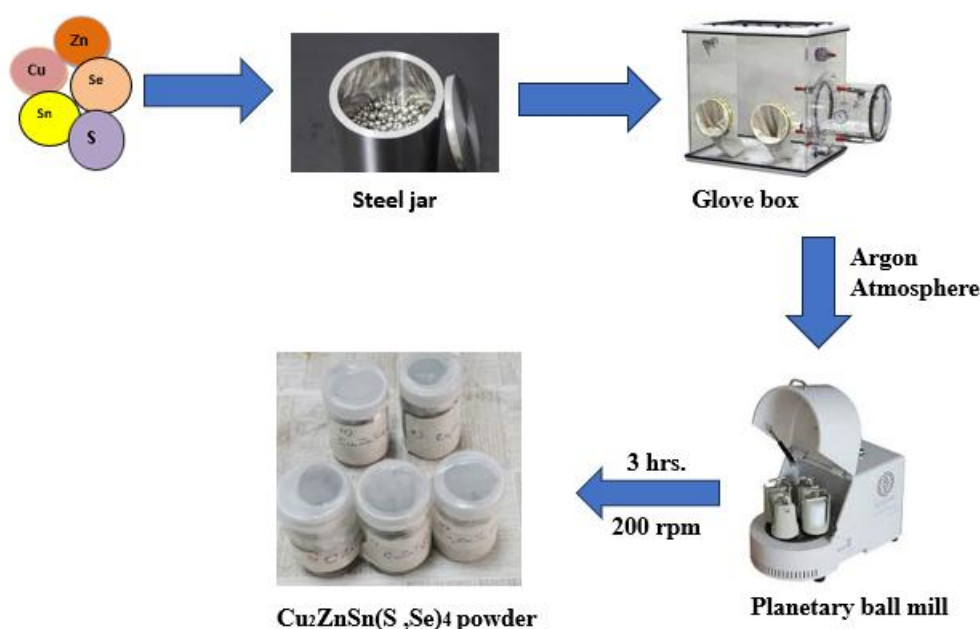
Figure 3.1 Synthesis process for the formation of $Cu_2ZnSnSSe_4$

3.3 Making of $Cu_2ZnSn(S,Se)_4$ pellets

Following the ball milling process, the resultant powders were gathered and further compacted into pellets using a manual hydraulic press machine. Three tons of pressure were applied for one minute during the hydraulic pressing process. Two types of pellets for five samples were made.

- Disk shape
- Bar shape

Disk pellets were made for thermal conductivity and other microstructural characterizations. The bar shaped pellets were made for electrical conductivity and Seebeck coefficient measurements.

After simple hydraulic pressing we have done CIP (cold isostatic pressing) of these pellets for further densification under the pressure of 6 ton for 4 min. The cold pressed pellets were placed in vacuum sealed quartz tubes and subjected to sintering in a tube furnace for a duration of 5 hours, maintaining a temperature of 500 K. This process was carried out in an inert atmosphere consisting of argon gas. Sintering was employed to make the dense pellet samples for improved thermoelectric properties.
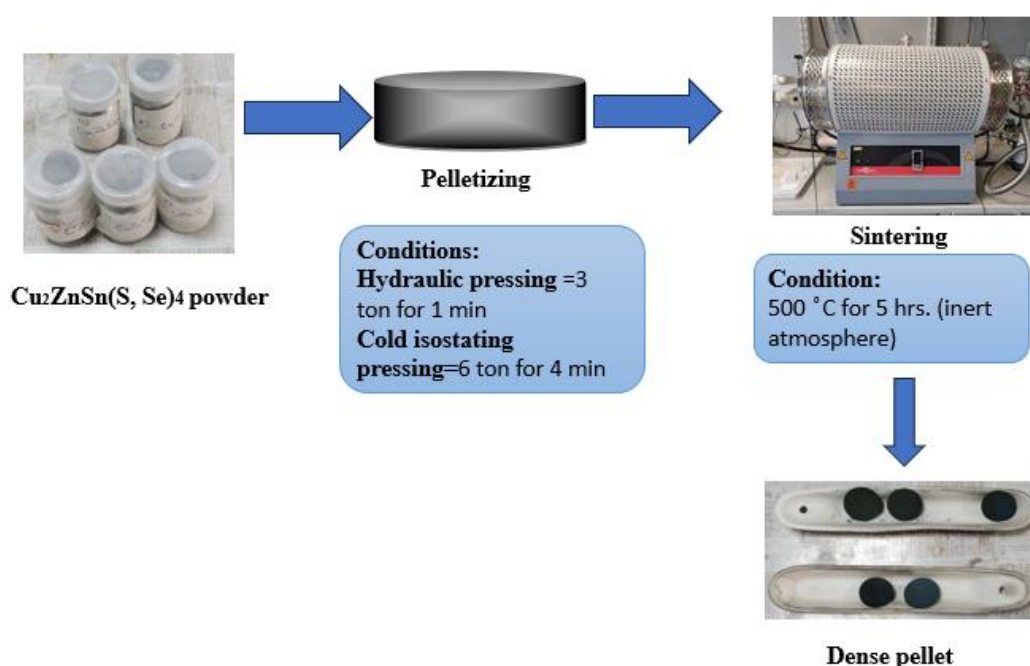
Figure 3.2 Pelletization of Cu$_2$ZnSn(S, Se)$_4$

Table 1 Elemental composition of Cu$_2$ZnSn (S$_x$, Se$_{1-x}$)$_4$ with different ratios

Elemental Precursors	X	Final composition
Cu$_2$ZnSn (S$_x$, Se$_{1-x}$)$_4$	0	Cu$_2$ZnSnSe$_4$
Cu$_2$ZnSn (S$_x$, Se$_{1-x}$)$_4$	0.1	Cu$_2$ZnSn (S$_{0.1}$, Se$_{0.9}$)$_4$

$Cu_2ZnSn (S_{x,} Se_{1-x})_4$	0.5	$Cu_2ZnSn (S_{0.5,} Se_{0.5})_4$
$Cu_2ZnSn (S_{x,} Se_{1-x})_4$	0.7	$Cu_2ZnSn (S_{0.7,} Se_{0.3})_4$
$Cu_2ZnSn (S_{x,} Se_{1-x})_4$	1	Cu_2ZnSnS_4

3.4 Characterization

There are multiple techniques that we used to characterize the $Cu_2ZnSn(S, Se)_4$. These techniques are given below:

- XRD
- SEM
- Thermal conductivity
- Electrical conductivity
- Seebeck analysis

3.4.1 X-ray Diffraction (XRD)

It is a common technique through which we can determine the crystalline phase of crystal structure. Crystalline phase indicates the characteristic peaks with different intensity levels. We can also determine the crystal structure, atomic spacing, lattice constants and unit cell dimension [66].
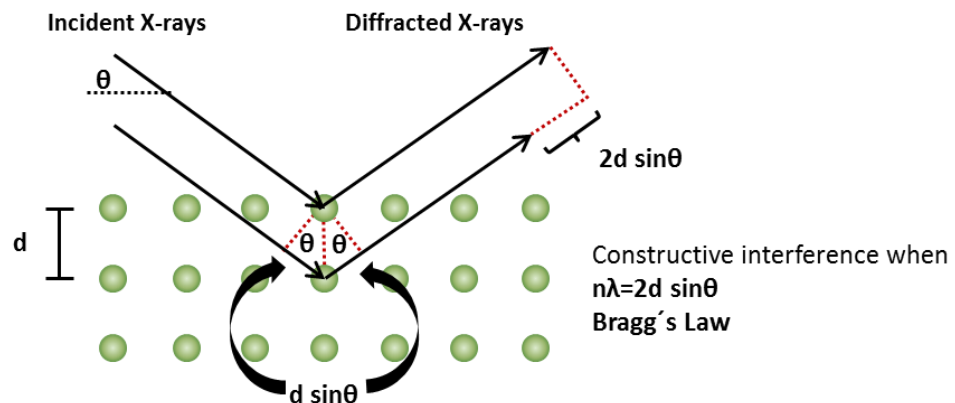
Figure 3.3 X-ray Diffraction.

X-ray diffraction is based on constructive interference of monochromatic X-ray and a crystalline sample. The sample, to be analyzed, should be ground to fine powder and homogenized. These X-rays are generated by the cathode ray tube, which produce

monochromatic radiation that are directed towards the material. When the conditions of Bragg's law satisfy the interaction of rays and material, result in constructive interference. The graph will be plotted between 2θ at x-axis and intensity at y-axis. The higher the peak of crystalline intensity level, the pure and crystalline the crystal is [67].

Bragg's law:

$$\textbf{2dsin}\boldsymbol{\theta} = \textbf{n } \boldsymbol{\lambda} \tag{1}$$

This law establishes a relationship between the wavelength of radiations, the lattice spacing, and the diffraction angle. We can identify the crystallites size from the given formula, known as Scherrer formula, named after Paul Scherrer.

Scherrer Equation [68]:

$$\textbf{D} = \frac{\textbf{K}\boldsymbol{\lambda}}{\boldsymbol{\beta}\textbf{Cos}\boldsymbol{\theta}} \tag{2}$$

We can determine the average crystalline size and size of a single crystal. In this equation,

D: crystallite size (nm).

k: Dimensionless shape factor with constant value of 0.94. It varies with the actual shape of crystalline.

λ: Wavelength of X-rays.

β: Full width half maximum value of spectra (radians).

θ: Bragg's angle (radians).

3.4.2 Scanning Electron Microscopy (SEM)

Scanning electron microscopy is a important method used to inspect and analyze various aspects of sample materials, such as their morphology, microstructure, size, shape, phase differences, and surface topography.

In SEM, an electron beam produced by a heated filament source (electron gun) is targeted and focused on surface of the sample using objective and condenser lenses. The focused electron beam then interacts with the sample, resulting in elastic or inelastic scattering processes.

By using SEM, researchers can gain precious insights into the properties and characteristics of materials at a microscopic level. This technique permits the imagining and examination of surface features, internal structures, and chemical composition, making it an indispensable tool in various scientific and industrial applications[69].
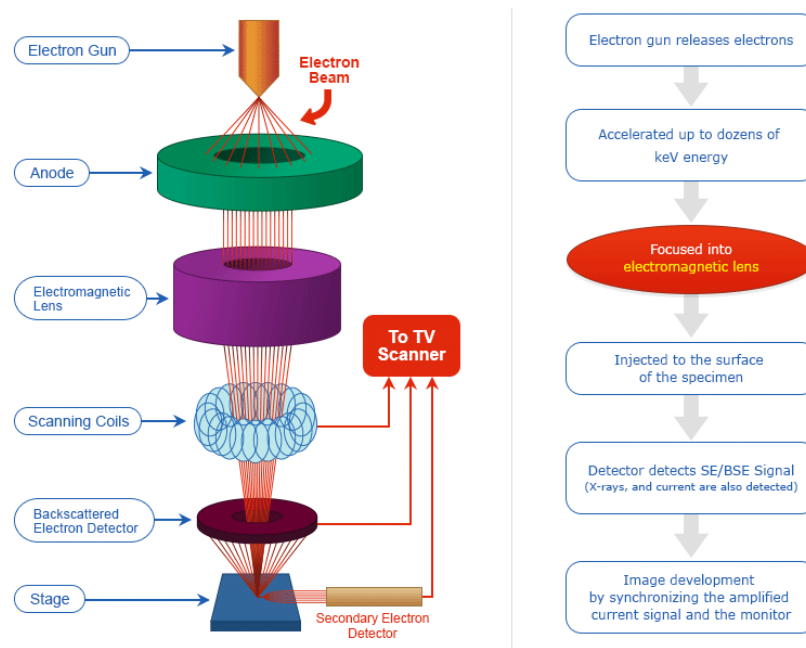
Figure 3.4 Schematic of SEM and detail of its various parts

The interaction between the electron beam and the sample in scanning electron microscopy (SEM) delivers valuable insights into the sample's characteristics, including morphology, external structure, chemical composition, and crystalline structure. The elastic interaction reveals compositional differences, while the inelastic interaction generates secondary electrons that show surface information. Our analysis of numerous samples was performed using the JEOL JSM-64900 SEM model, which allows us to investigate and characterize materials at a micro- and nanoscale level [70].
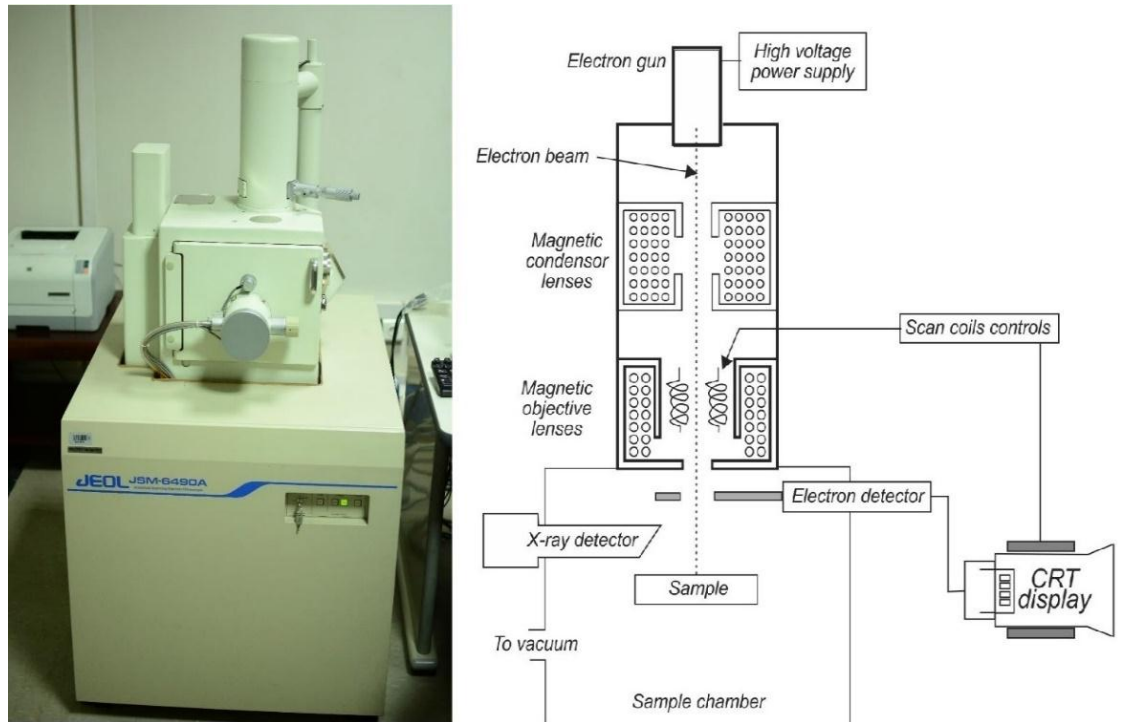
Figure 3.5 JEOL JSM 6490A figure and schematic

3.4.3 Energy Dispersive X-ray (EDX)

Energy Dispersive X-ray Spectroscopy (EDX or EDS) is an analytical technique used to determine the elemental composition of a sample. It is commonly employed in conjunction with scanning electron microscopy (SEM).

The EDX technique involves the utilization of a concentrated electron beam that is directed towards the surface of the specimen, resulting in interactions with the constituent atoms. These interactions result in the release of characteristic X-rays that possess energies that are unique to the individual elements found within the sample. The X-rays that are emitted are then detected and subjected to analysis, so yielding valuable insights on the composition of the sample, including the identification and quantification of various elements present. EDX is non-destructive, allowing multiple analyses on the same sample without altering its integrity. It is widely used for qualitative and quantitative elemental analysis in various fields, such as materials science, geology, metallurgy, electronics, and forensics. The technique is valuable for identifying unknown materials, verifying material compositions, studying surface coatings, and investigating the distribution of elements within a sample.
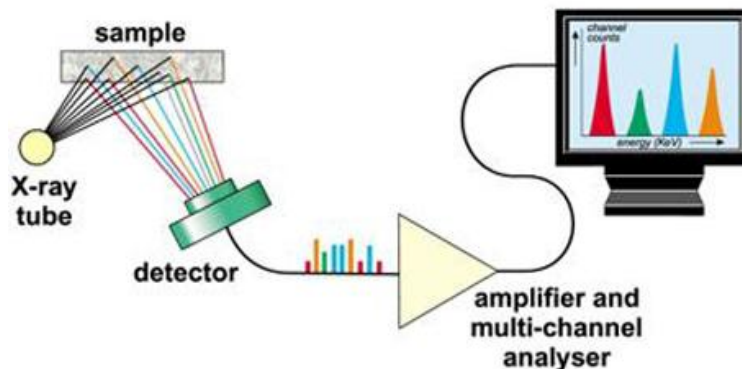
Figure 3.6 Schematic diagram of EDX.

3.4.4   UV -Visible Spectroscopy

Ultraviolet-Visible spectroscopy is a spectroscopic technique that primarily involves the measurement of absorption or reflection in the ultraviolet and visible regions of the electromagnetic spectrum. Electronic transitions occur in atoms and molecules within the ultraviolet and visible spectrum. The basic principle of UV-VIS absorption is that molecules containing electrons that absorb energy in the form of visible and ultraviolet light sources, are used to stimulate the electrons towards the higher orbit. The electrons that are easily excited from lower energy band gap have a longer light absorption wavelength. When the light is passing through the sample the intensity is measured and then compared to the reference sample which in our case was DI water.

The main parts of this instrument are the light source and sample holder, a prism, and a detector. Tungsten filament is the common source of photons, while deuterium arc lamp is also used in some systems. The detector used in this spectroscopy is basically a photomultiplier tube.

The sample can be prepared in the form of suspension. A small amount of thick suspension is mixed in DI water and transferred to the cuvettes. Then the cuvettes are placed in the instrument. One cuvette is placed as a reference sample.

Figure 3.7 UV-Vis Spectroscopy

3.4.5 Laser Flash Analysis (LFA)

The Laser Flash Analysis (LFA) is used to measure the thermal diffusivity of various materials. In this test, a sample is placed inside tube-like structure, and a laser flash is applied to one side of the sample. As a result, the temperature on the front side of the sample increases, and this temperature change travels through the material towards the opposite side. Infrared detectors in the setup record this temperature variation. The time it takes for the heat to reach the rear end of the sample depends on the material's diffusivity. Higher thermal diffusivity leads to a shorter time for the heat to reach the back end.

Thermal diffusivity is a material property that varies among different materials and is employed to describe how efficiently they conduct heat under changing or unsteady temperature conditions. It indicates the material's ability to quickly respond to temperature fluctuations.

To calculate thermal conductivity, the thermal diffusivity is combined with density and heat capacity using the following formula:

$$\kappa = \alpha * \rho * C_s$$

Where κ, α, ρ, and C_s represents thermal conductivity, thermal diffusivity, density, and specific heat capacity respectively.
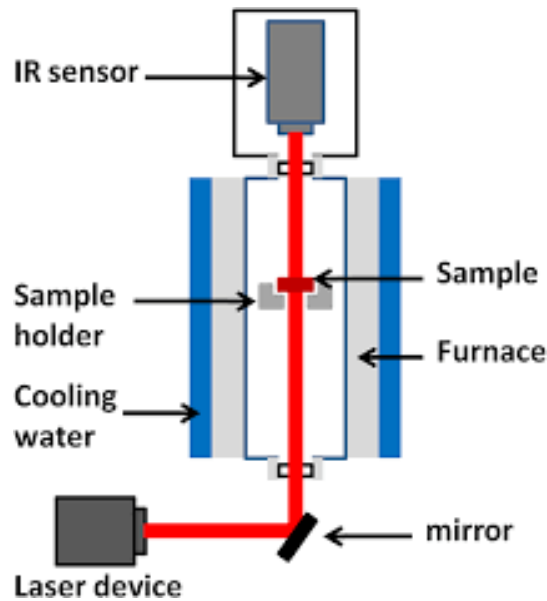
Figure 3.8 Laser flash analysis schematics

3.4.6 Seebeck Analysis

The Seebeck effect is an experimental process where we test a material by heating one end and keeping the other end cool. This creates a temperature difference between the two ends, resulting in the generation of an electric voltage.

$$S = \frac{\Delta V}{\Delta T}$$

We measure this voltage while varying the temperature difference and plot the data on a graph. The slope of the graph gives us the Seebeck coefficient, which represents how efficient the material is in converting heat to electricity. To ensure accurate measurements, we may use temperature compensation techniques to nullify any initial temperature differences. The Seebeck effect helps us understand the relationship between temperature and electricity in different materials and is essential for designing thermoelectric devices and temperature sensors.
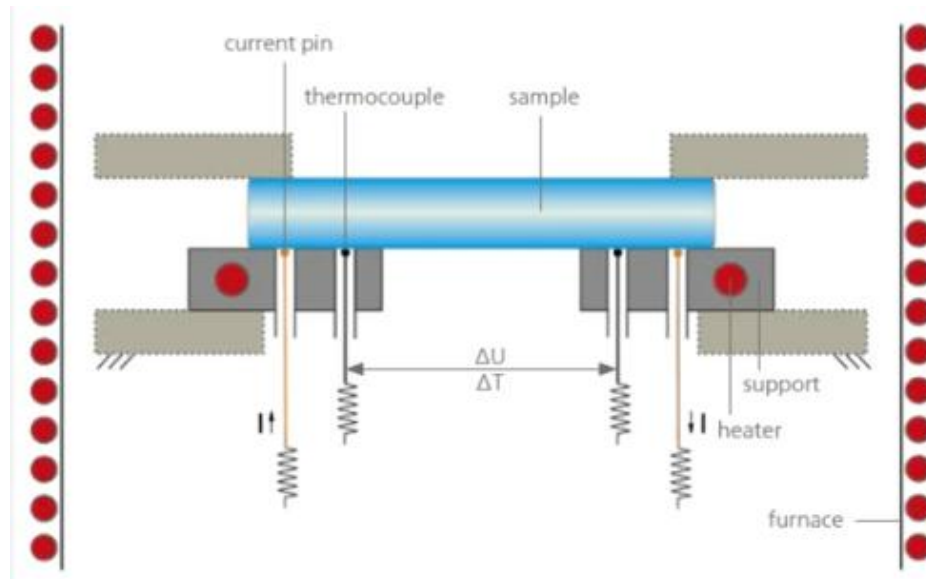
Figure 3.9 Seebeck analysis schematics

3.4.7 Electrical Conductivity

The four-probe method is a highly accurate and essential technique for determining the electrical conductivity and resistivity of materials, particularly for thin films and materials with small dimensions. It offers distinct advantages over conventional two-probe measurements by eliminating the impact of contact resistances, ensuring reliable and precise results.

In this method, four evenly spaced electrical contacts are strategically placed on the material's surface. Two inner probes serve as current-carrying electrodes, while two outer probes act as voltage detectors. By applying a known direct current (DC) through the inner probes, an electric field is induced within the material, leading to a measurable voltage drop across the sample.

The voltage drop is carefully measured using the outer probes, and the data obtained is then analyzed using Ohm's law. The resistivity (ρ) of the material is calculated using the formula: Resistivity (ρ) = (V * π * L) / (I * R), where V represents the voltage drop, I is the applied current, L is the distance between the voltage probes, and R denotes the geometric factor specific to the four-probe configuration.

Once the resistivity is determined, the electrical conductivity (σ) of the material is easily obtained through the equation:

Electrical Conductivity (σ) = 1 / ρ

Chapter 4

4 Results and Discussion

4.1 X-Ray Diffraction

The structural analysis was done through X-ray diffractometer (Model STOE θ-θ). Figure 4.1 presents the XRD patterns of $Cu_2ZnSn(S_x,Se_{1-x})_4$ (CZTSSe, $0 \leq x \leq 1$). The graph shows diffraction peaks at angle 2θ values 28.51, 32.89, 47.24 and 55.98 with reflection from (112), (200), (220), and (312) planes respectively.

As the S content increases, the major peaks (112), (220), and (312) in all samples shift towards higher angles. The shift of the major peaks towards higher angles as the S content increases, ranging from 0% to 100%, reveals a continuous transformation in the CZTSSe phase. Specifically, the diffraction peaks gradually move to higher angles, which signifies the transition from stannite CZTSe to kesterite CZTS. The reason for this shift is the substitution of larger Se atoms (190pm) with smaller S atoms (180pm). This substitution results in a reduction of the interplanar spacings. Importantly, no additional peaks from secondary phases were observed in the XRD patterns, further confirming the purity of samples. These findings are consistent with the data from the JCPDS cards no: 00-026-0575 and 00-052-0868. Therefore, the observed diffraction peaks and interplanar spacing of CZTSSe provide strong evidence for the formation of kesterite and stannite phases, which is dependent on the Se and S content in the sample.

The average crystallite size of the samples were determined using Scherrer's formula. Interestingly results revealed a significant trend as the S content increases the average crystal size decreases. The results are shown in table 2.
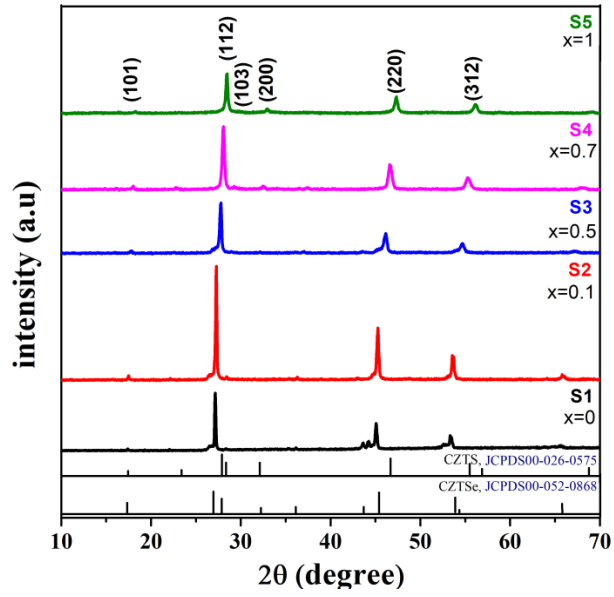
Figure 4.1 XRD analysis of Cu$_2$ZnSn(S$_x$, Se$_{1-x}$)$_4$

Table 2 Avg. crystallite size of Cu$_2$ZnSn(S$_x$, Se$_{1-x}$)$_4$ samples

Sample No.	Sample Composition	FWHM degrees	2θ degrees	Avg Crystallite Size (D)
S1	Cu$_2$ZnSnSe$_4$	0.14972	27.15241	
		0.24702	45.07941	
		0.34896	53.39708	39.997
S2	Cu$_2$ZnSn(S$_{0.1}$Se$_{0.9}$)$_4$	0.14979	27.26322	
		0.28765	45.25259	
		0.37263	53.62708	37.732
S3	Cu$_2$ZnSn(S$_{0.5}$Se$_{0.5}$)$_4$	0.27558	27.75225	
		0.53003	46.09536	
		0.72458	54.63935	20.304
S4	Cu$_2$ZnSn(S$_{0.7}$Se$_{0.3}$)$_4$	0.32596	28.05398	
		0.52227	46.63457	
		0.65937	55.31276	19.247
S5	Cu$_2$ZnSnS$_4$	0.32158	28.44265	
		1.55157	32.97204	
		0.50355	47.30658	
		0.58996	56.13017	20.181

4.2 Scanning Electron Microscopy

Figure 4.2 displays the SEM images of $Cu_2ZnSn(S_x, Se_{1-x})_4$ ($0 \leq x \leq 1$). Images showed that CZTSSe exhibit a uniform distribution and possesses a nano-sized scale, indicating that they display consistent and evenly dispersed characteristics at the nano scale level. The size range of these $CZT(S, Se)_4$ powders is under 36nm.

S1

S2

20kV X50,000 0.5μm   SCME NUST
20kV X50,000 0.5μm   SCME NUST

S4

20kV X60,000 0.2μm   SCME NUST
20kV X50,000 0.5μm   SCME NUST

S5

20kV X60,000 0.2μm   SCME NUST
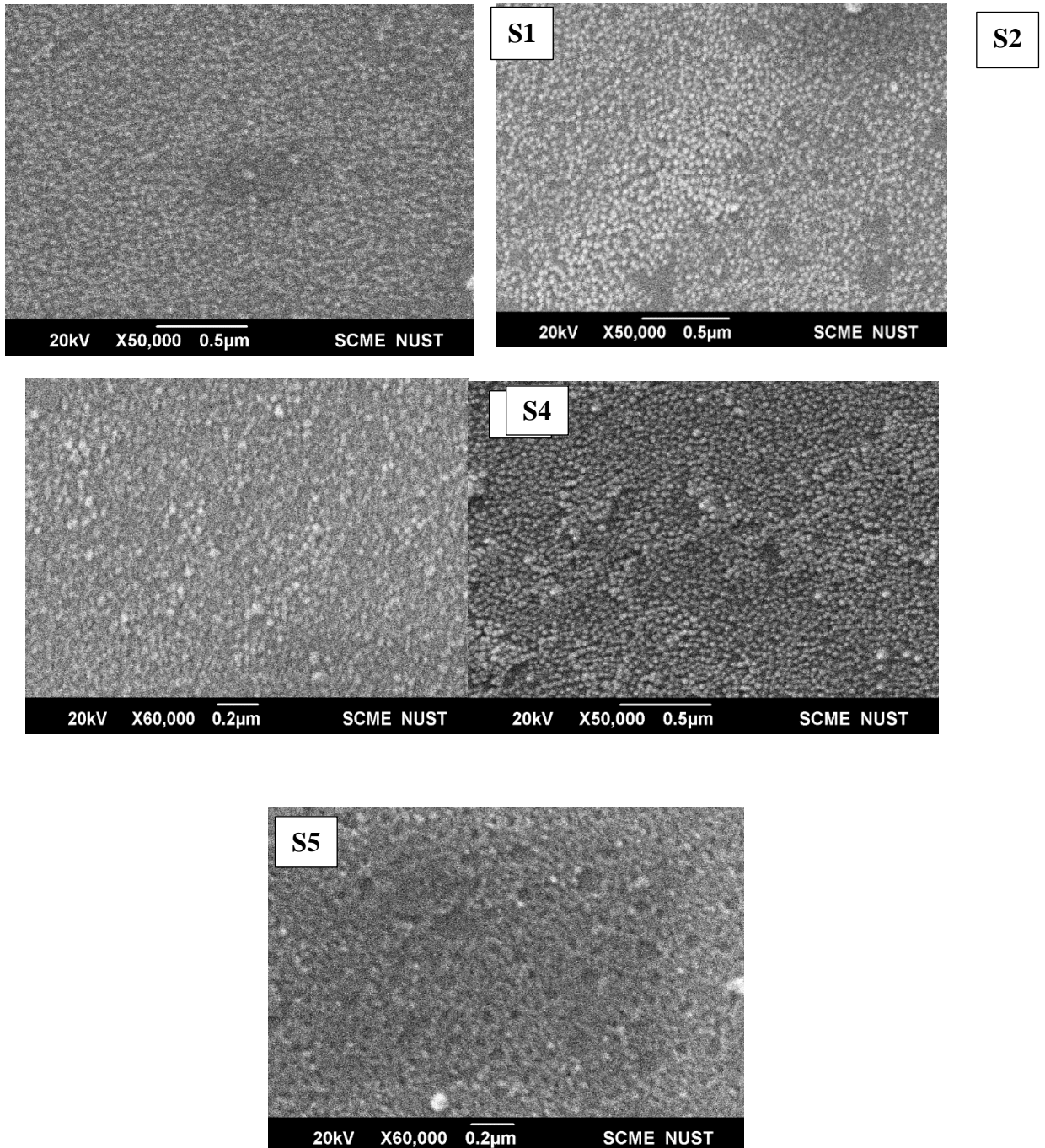
Figure 4.2 SEM micrographs of $Cu_2ZnSn(S_x, Se_{x-1})_4$

4.3 Energy dispersive x-ray spectroscopy (EDX)

EDX measurements were employed to investigate the elemental composition of $Cu_2ZnSn(S_x,Se_{1-x})_4$. The table represents atomic percentage & weight percentage of elements at different stochiometric ratios.

Table 3 Elemental compositional analysis

Sample No.	X	Composition	Elements	% Atomic	% Weight
S1	0	$Cu_2ZnSnSe_4$	**Copper**	23	18.6
			Zinc	12.6	10.5
			Tin	12	18.2
			Selenium	52.4	52.7
S2	0.1	$Cu_2ZnSn(S_{0.1}Se_{0.9})_4$	**Copper**	25.3	25.5
			Zinc	12.7	13.6
			Tin	11.6	19.4
			Sulfur	24.4	12
			Selenium	26	29.5
S3	0.5	$Cu_2ZnSn(S_{0.5}Se_{0.5})_4$	**Copper**	26.9	25.5
			Zinc	13.4	13
			Tin	10.4	18.5
			Sulfur	21.5	10.3
			Selenium	27.8	32.7
S4	0.7	$Cu_2ZnSn(S_{0.7}Se_{0.3})_4$	**Copper**	33	36.2
			Zinc	22.3	25.1
			Tin	4.4	9.1
			Sulfur	31.2	17.2
			Selenium	9.1	12.5
S5	1	Cu_2ZnSnS_4	**Copper**	46	46.5
			Zinc	9.3	9.7
			Tin	15.3	28.9
			Sulfur	29.4	15

4.4 Bandgap Analysis

Figure 4.3, displays the band gap values of different compositions of $Cu_2ZnSn(S_x,Se_{1-x})_4$. The determination of the band gap was conducted by directly calculating it based on the absorption maxima observed in the UV Vis Spectroscopy absorption spectra. In more detail, the absorption peak in UV is considered as the point where electrons are going to the excited state from its ground state at their specific optical band gap.

Energy equation of quantum mechanics:

*Energy (E) = Planks Constant (h) * Speed of Light (C) / Wavelength (λ)*

Where,

Energy (E) = Band gap,

Planks constant (h) = 6.626×10^{-34} Joules sec,

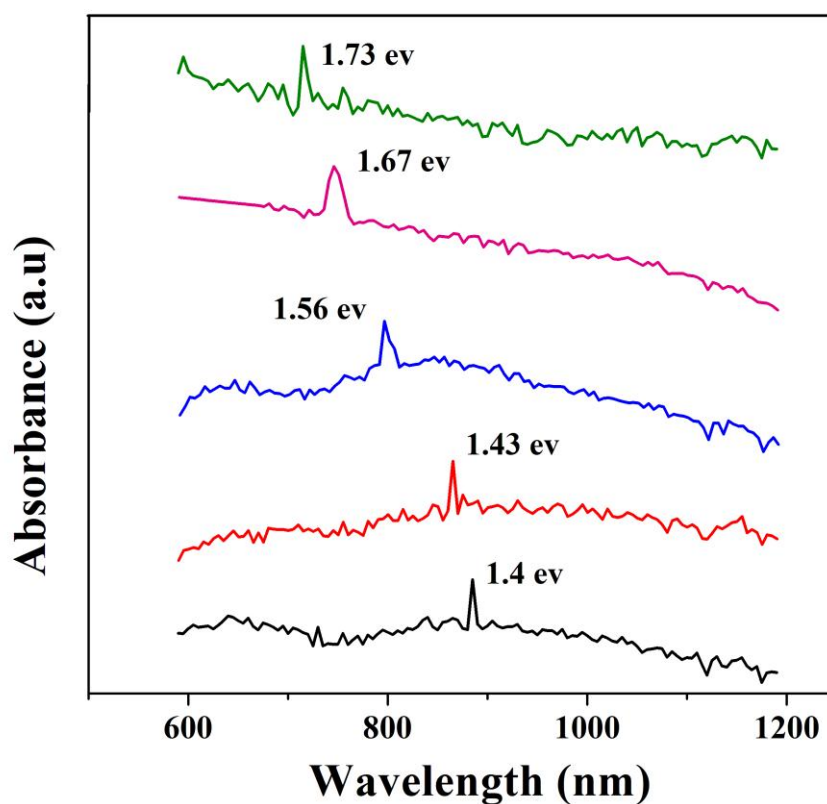Velocity of Light (C) = 2.99×10^8 meter/sec and Wavelength (λ) = Absorption peak

Figure 4.3 Change in UV-vis absorption spectra of $Cu_2ZnSn(S_x, Se_{1-x})_4$

value. While 1eV = 1.6×10^{-19} Joules (is a conversion factor)

Using this formula, band gaps were determined based on the peak value obtained from UV-Vis spectroscopy absorption peaks. This material possesses the unique property of compositional tunability, enabling the adjustment of its band gap within a range from 1.4 eV to 1.73 eV. When considering $Cu_2ZnSnSe_4$, it exhibits a narrow band gap of approximately 1.4 eV, a value that aligns well with previously reported experimental data. On the other hand, as the S content increases in $Cu_2ZnSn(S, Se)_4$ by replacing Se atoms, the band gap also increases. When S completely replaces Se in the material, the band gap of Cu_2ZnSnS_4 reaches a value of approximately 1.73 eV. Consequently, an increased band gap in $Cu_2ZnSn(S_x,Se_{1-x})_4$, achieved through the incorporation of S, leads to a reduction in the number of available charge carriers (electrons and holes) for conduction. This, in turn, results in lower electrical conductivity.

4.5 Thermoelectric Properties

Figure 4.3(a) illustrates the electrical conductivity of $Cu_2ZnSn(S_x, Se_{1-x})_4$ within the temperature range of 300 K to 600 K. Notably, as the measuring temperature rises, the electrical conductivity exhibits a decreasing trend, indicating semi-metallic behavior. However, intriguing anomalies are observed in samples S2 and S5, where the electrical conductivity initially increases at 400 K and subsequently decreases, deviating from the overall trend. These variations in electrical conductivity can be attributed to the presence of different bond lengths and bond energies in $Cu_2ZnSn(S_x, Se_{1-x})_4$, particularly due to the bond variations of S and Se. The trend highlights that the electrical conductivity of sample S5 is relatively lower compared to other samples because of large band gap and also discrepancy in electrical conductivity is mainly attributed to the presence of sulfur in S5, while S1 exhibits higher electrical conductivity mainly due to the narrow band gap compared with other samples.

The different atomic radius and electronegativity of sulfur and selenium atoms result in varying bond lengths and bond energies between Cu-S, Zn-S, Sn-S in (Cu_2S_4), $(SnZnS_4)$ layers, and Cu-Se, Zn-Se, Sn-Se in (Cu_2Se_4), $(SnZnSe_4)$ layers. These

variations impact the mobility properties in the CZTSSe crystal structure. For instance, in the case of S2 (x=0.1), the electrical conductivity increases from 3.9 x 10^3 S m^{-1} at 300 K to 4.8 x 10^3 S m^{-1} at 400 K, and then decreases to 3.1 x 10^3 S m^{-1} at 600 K. This behavior indicates that the incorporation of sulfur in the CZTSe lattice results in CZTSSe (x=0.1) exhibiting different carrier transport mechanisms between the (Cu_2Se_4) layers, which act as electrical conductors, and ($SnZnSe_4$) layers, which also contribute to electrical conduction. This behavior arises due to the formation of tetrahedral ($Cu_2(S,Se)_4$) layers and ($SnZn(S,Se)_4$) layers.
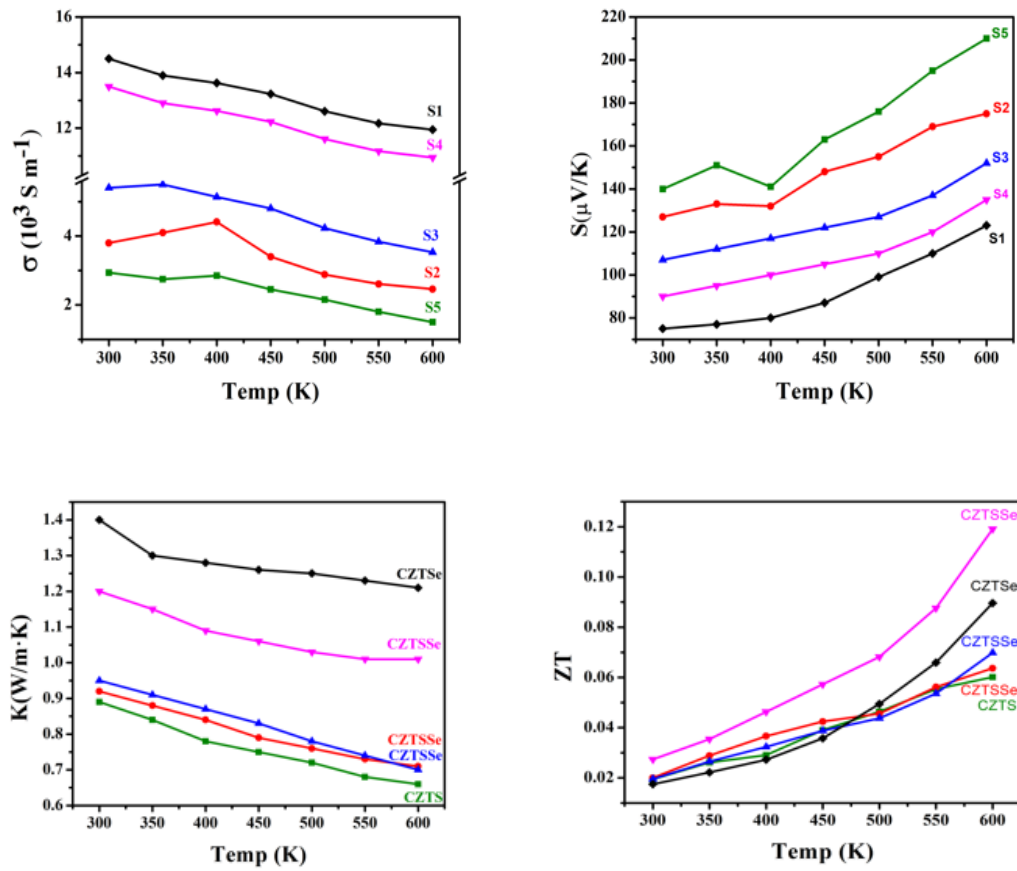
Figure 4.3 (a) Electrical conductivity (b) Seebeck coefficient (c) Thermal conductivity (d) Figure of merit of Cu_2ZnSn (S_x, Se_{1-x})$_4$ at x=0, 0.1, 0.5, 0.7, 1

According to Figure 4.3(b), all $Cu_2ZnSn(S_x, Se_{1-x})4$ ($0 \leq x \leq 1$) exhibit positive Seebeck throughout the entire temperature range, indicating that they are all p-type semiconductors. Additionally, the Seebeck values of CZTSSe with different x

increase from 300 K to 600 K, except for a slight decrease observed from 350 K to 400 K in samples S2 and S5. This phenomenon is attributed to the distribution of most holes into high energy states. At 600 K, the Seebeck value for S5 reaches around 212 µV/K, the highest among all the samples. This high Seebeck value in S5 is mainly due to its low carrier concentration, as predicted by the Mott formula:

$$S = \frac{8\pi k_\beta T}{3qh^2} m^* \left(\frac{\pi}{3n}\right)^{\frac{2}{3}}$$

Where k_β is Boltzmann constant, q is charge carrier, h is Planks constant, m^* is effective mass and n is carrier concentration. The formula indicates that Seebeck is inversely proportional to carrier concentration. Thus, the higher Seebeck value in S5 is a result of its lowest electrical conductivity.

On the other hand, the Seebeck value for S1 is comparatively lower across the temperature range of 300 K to 600 K, mainly due to its high electrical conductivity. To increase the Seebeck values, it is suggested to either dope Cu ions into the CZTSSe lattice or substitute Zn with elements like Cd, Mn, Fe, or Co. [71].

Figure 4.3(c) displays the thermal conductivity graph of $Cu_2ZnSn(S_x, Se_{1-x})_4$ ($0 \leq x \leq 1$). The graph clearly reveals a distinct decrease in thermal conductivity (K) as the temperature range extends from 300K to 600K. Among all the samples, S1 exhibits the highest thermal conductivity, mainly attributed to the presence of selenium content. Selenium is known to possess high thermal conductivity characteristics. Conversely, samples S2, S3, S4, and S5 exhibit lower thermal conductivity due to the presence of insulative bonds induced by the sulfur content. The results strongly suggest that the thermal conductivity of S5 is the lowest among all the samples studied as it has highest amount of Sulfur content which act as thermal barrier, hence lowering the total thermal conductivity.

In Figure 4.3(d), the graph illustrates the ZT values of $Cu_2ZnSn(S_x, Se_{1-x})_4$ ($0 \leq x \leq 1$). The thermoelectric figure of merit (ZT) is determined by the equation $ZT = \frac{S^2 \sigma T}{k}$, where S represents the Seebeck coefficient, σ is the electrical conductivity, k denotes the thermal conductivity, and T stands for the absolute temperature. As the temperature increases, the ZT values show a noticeable rise across the samples. Particularly, sample S4 consistently exhibits higher ZT values compared to other samples. At 600 K, the ZT for S4 reaches 0.12, which is the highest among all the

samples. This higher ZT in S4 can be attributed to its favorable electrical conductivity and reasonable Seebeck coefficient, which contribute to the overall enhancement.

Conclusion

In this study, we utilized the mechanochemical alloying technique, followed by heat treatment, to achieve the successful synthesis of quaternary chalcogenides CZTSSe. Through rigorous analysis using X-ray diffraction (XRD) and energy-dispersive X-ray spectroscopy (EDX), we confirmed the transformation from CZTSe stannite to CZTS kesterite phase by increasing the sulfur content in CZTSe. Our investigation focused on analyzing the band gap and thermoelectric properties. To accomplish this, we conducted measurements of electrical conductivity, thermal conductivity, and Seebeck coefficient within a temperature range of 300 to 600 K.

Our findings reveal intriguing trends in the thermoelectric properties of CZTSSe based on varying sulfur content. As the percentage of sulfur in CZTSe increases, electrical conductivity decreases due to a transition from conductive bonds to insulative bonds. Moreover, the increase in sulfur content leads to a wider band gap, which further reduces electrical conductivity. Interestingly, the Seebeck coefficient shows an opposite trend, increasing with higher sulfur content. This effect is primarily attributed to the low carrier concentration resulting from the increase in sulfur content. Additionally, the presence of sulfur acts as an insulator in Cu-S, Zn-S, and Sn-S bonds, leading to a decrease in thermal conductivity as the sulfur content increases. We calculated the dimensionless figure of merit (ZT) to assess the overall thermoelectric performance of the samples. Notably, sample S4 exhibited the highest ZT value of 0.12, owing to its intermediate properties compared to other samples. Importantly, these ZT values are comparable to those reported for compounds synthesized using solid-state techniques, demonstrating the promising potential of the CZTSSe compounds in thermoelectric applications.

In summary, our study highlights the significant influence of different sulfur and selenium ratios in the solid solution on the thermoelectric properties of CZTSSe. These findings contribute to a better understanding of the underlying mechanisms

affecting the performance of these compounds and offer valuable insights for further improvements and applications in thermoelectric devices.

References

[1]   Chen, Z.-G., et al., *Nanostructured thermoelectric materials: Current research and future challenge.* Progress in Natural Science: Materials International, (2012). **22**(6): p. 535-549.

[2]   Liu, W., et al., *New trends, strategies and opportunities in thermoelectric materials: A perspective.* Materials Today Physics, (2017). **1**: p. 50-60.

[3]   Kumar, S., et al., *Thermoelectric generators for automotive waste heat recovery systems part I: numerical modeling and baseline model analysis.* (2013). **42**: p. 665-674.

[4]   Dresselhaus, M.S., et al., *New directions for low‐ dimensional thermoelectric materials.* (2007). **19**(8): p. 1043-1053.

[5]   Liu, W., et al., *Recent advances in thermoelectric nanocomposites.* (2012). **1**(1): p. 42-56.

[6]   Saravanan, R., *Manufacturing optimization through intelligent techniques.* (2006): CRC Press.

[7]   Liu, X., *High-Performance Bi2Te3-Based Thermoelectric Materials: Fundamentals, Fabrication, and Characterisation.* (2017).

[8]   Boyer, A., E.J.M.S. Cisse, and E. B, *Properties of thin film thermoelectric materials: application to sensors using the Seebeck effect.* (1992). **13**(2): p. 103-111.

[9]   Jia, B., et al., *Study on thermoelectric properties of co-evaporated Sn-Se films with different phase formations.* (2019). **672**: p. 133-137.

[10]   Caroff, T., et al., *New optimization strategy of thermoelectric coolers applied to automotive and avionic applications.* (2015). **2**(2): p. 751-760.

[11]   Belov, I., V. Volkov, and O. Manyakin. *Optimization of Peltier thermocouple using distributed Peltier effect.* in *Eighteenth International Conference on Thermoelectrics. Proceedings, ICT'99 (Cat. No. 99TH8407).* (1999).

[12] Jin, W., et al., *Exploring Peltier effect in organic thermoelectric films.* (2018). **9**(1): p. 3586.

[13] Huang, M.-J., et al., *The influence of the Thomson effect on the performance of a thermoelectric cooler.* (2005). **48**(2): p. 413-418.

[14] Lashkevych, I., et al., *Special important aspects of the Thomson effect.* (2018). **47**: p. 3189-3192.

[15] Snyder, G.J., A.H.J.E. Snyder, and E. Science, *Figure of merit ZT of a thermoelectric device defined from materials properties.* (2017). **10**(11): p. 2280-2283.

[16] Baliga, B.J.J.I.E.D.L., *Power semiconductor device figure of merit for high-frequency applications.* (1989). **10**(10): p. 455-457.

[17] Xia, C. and J.J.J.o.S. Li, *Recent advances in optoelectronic properties and applications of two-dimensional metal chalcogenides.* (2016). **37**(5): p. 051001.

[18] Ding, Y., et al., *Transport properties and high thermopower of SnSe2: a full ab-initio investigation.* (2017). **121**(1): p. 225-236.

[19] Jalil, O., et al., *Towards theoretical framework for probing the accuracy limit of electronic transport properties of SnSe2 using many-body calculations.* (2020). **130**(5): p. 57001.

[20] Yingchun, D., et al., *Transport Properties and High Thermopower of SnSe2: A Full Ab-Initio Investigation.* (2017).

[21] Junior, O.A., et al., *A review of the development and applications of thermoelectric microgenerators for energy harvesting.* (2018). **91**: p. 376-393.

[22] Ding, G., et al., *A comparative study of thermoelectric properties between bulk and monolayer SnSe.* (2019). **15**: p. 102631.

[23] Snyder, G.J. and E.S.J.N.m. Toberer, *Complex thermoelectric materials.* (2008). **7**(2): p. 105-114.

[24] Zoppi, G., et al., *Cu2ZnSnSe4 thin film solar cells produced by selenisation of magnetron sputtered precursors.* (2009). **17**(5): p. 315-319.

[25] Chichibu, S.F., et al., *Fabrication of p-CuGaS2/n-ZnO: Al heterojunction light-emitting diode grown by metalorganic vapor phase epitaxy and helicon-wave-excited-plasma sputtering methods.* (2005). **66**(11): p. 1868-1871.

[26]   Ouahrani, T., et al., *Ab-initio study of the structural, linear and nonlinear optical properties of CdAl2Se4 defect-chalcopyrite.* (2010). **183**(1): p. 46-51.

[27]   Fan, F.-J., et al., *Colloidal synthesis of Cu2CdSnSe4 nanocrystals and hot-pressing to enhance the thermoelectric figure-of-merit.* (2011). **133**(40): p. 15910-15913.

[28]   Matsushita, H., T. Ichikawa, and A.J.J.o.m.s. Katsui, *Structural, thermodynamical and optical properties of Cu 2-II-IV-VI 4 quaternary compounds.* (2005). **40**: p. 2003-2005.

[29]   Liu, M.L., et al., *Improved thermoelectric properties of Cu‐ doped quaternary chalcogenides of Cu2CdSnSe4.* (2009). **21**(37): p. 3808-3812.

[30]   Tiwari, K.J., et al., *Ball mill synthesis of bulk quaternary Cu 2 ZnSnSe 4 and thermoelectric studies.* (2017). **46**: p. 30-39.

[31]   He, J., et al., *Composition dependence of structure and optical properties of Cu2ZnSn (S, Se) 4 solid solutions: an experimental study.* (2012). **511**(1): p. 129-132.

[32]   Zuhud, A.M., F. Mochammad, and W. Widayat. *Thermoelectric application in energy conservation*. in *E3S Web of Conferences*. (2018). EDP Sciences.

[33]   Brignone, M. and A. Ziggiotti. *Impact of novel thermoelectric materials on automotive applications*. in *AIP Conference Proceedings*. (2012). American Institute of Physics.

[34]   Shi, X., L. Chen, and C.J.I.M.R. Uher, *Recent advances in high-performance bulk thermoelectric materials.* (2016). **61**(6): p. 379-415.

[35]   Date, A., et al., *Progress of thermoelectric power generation systems: Prospect for small to medium scale power generation.* (2014). **33**: p. 371-381.

[36]   Wang, Z., et al., *Realization of a wearable miniaturized thermoelectric generator for human body applications.* (2009). **156**(1): p. 95-102.

[37]   Liu, H., et al. *Design of a wearable thermoelectric generator for harvesting human body energy*. in *Wearable Sensors and Robots: Proceedings of International Conference on Wearable Sensors and Robots 2015*. (2017). Springer.

[38]   Zhao, D. and G. Tan, *A review of thermoelectric cooling: Materials, modeling and applications.* Applied Thermal Engineering, (2014). **66**(1): p. 15-24.

[39]   Yin, Y., B. Tudu, and A.J.V. Tiwari, *Recent advances in oxide thermoelectric materials and modules.* (2017). **146**: p. 356-374.

[40]   Haacke, G.J.J.o.A.p., *New figure of merit for transparent conductors.* (1976). **47**(9): p. 4086-4089.

[41]   Yang, C.C. and S.J.C. Li, *Basic Principles for Rational Design of High‐ Performance Nanostructured Silicon‐ Based Thermoelectric Materials.* (2011). **12**(18): p. 3614-3618.

[42]   Masood, K.B., et al., *Odyssey of thermoelectric materials: foundation of the complex structure.* (2018). **2**(6): p. 062001.

[43]   Xu, P., et al., *Anisotropic thermoelectric properties of layered compound SnSe2.* (2017). **62**(24): p. 1663-1668.

[44]   Yamamoto, A. and T. Ohta. *Thermoelectric figure of merit of silicide two-dimensional quantum wells*. in *IECEC 96. Proceedings of the 31st Intersociety Energy Conversion Engineering Conference*. 1996. IEEE.

[45]   Zhang, X. and L.-D. Zhao, *Thermoelectric materials: Energy conversion between heat and electricity.* Journal of Materiomics, (2015). **1**(2): p. 92-105.

[46]   Song, X., et al., *A Review on Development Prospect of CZTS Based Thin Film Solar Cells.* International Journal of Photoenergy, (2014). p. 613173.

[47]   Gao, F., et al., *Structural and Optical Properties of In-Free Cu2ZnSn(S,Se)4 Solar Cell Materials.* Japanese Journal of Applied Physics, (2012). **51**(10S): p. 10NC29.

[48]   Tiwari, K.J., et al., *Ball Mill Synthesis of Bulk Quaternary Cu2ZnSnSe4 and Thermoelectric Studies.* Journal of Electronic Materials, (2017). **46**(1): p. 30-39.

[49]   He, J., et al., *Composition dependence of structure and optical properties of Cu2ZnSn(S,Se)4 solid solutions: An experimental study.* Journal of Alloys and Compounds, (2012). **511**(1): p. 129-132.

[50]   Chinnaiyah Sripan, Annamraju Kasi Viswanath, and G. R, *Effect of excess selenium in the formation of Cu2Zn1.5Sn1.2(S0.9 + Se0.1)4 alloys for solar cell applications.* Nanosystems: Physics, Chemistry, Mathematics, (2016) (3): p. 509–512.

[51]   Cao, V.M., et al. *Fabrication of the Cu2ZnSnS4 Thin Film Solar Cell via a Photo-Sintering Technique*. Applied Sciences, (2022). **12**, DOI: 10.3390/app12010038.

[52]   Pani, B., S. Pillai, and U.P. Singh, *Kesterite based thin film absorber layers from ball milled precursors.* Journal of Materials Science: Materials in Electronics, (2016). **27**(12): p. 12412-12417.

[53]   Farva, U. and C. Park, *Quaternary Chalcogenide Nanocrystals: Synthesis of Cu2ZnSnSe4 by Solid State Reaction and their Thermoelectric Properties.* MRS Online Proceedings Library (OPL), (2013). **1543**: p. 137-142.

[54]   Solovan, M.N., et al., *Structural and optical properties of Cu2ZnSn(S,Se)4 films obtained by magnetron sputtering of a Cu2ZnSn alloy target.* Physics of the Solid State, (2017). **59**(8): p. 1643-1647.

[55]   Sahu, M., et al. *Synthesis and Characterization of Cu2ZnSnSe4 by Non-Vacuum Method for Photovoltaic Applications*. Nanomaterials, (2022). **12**, DOI: 10.3390/nano12091503.

[56]   Guo, Q., H.W. Hillhouse, and R. Agrawal, *Synthesis of Cu2ZnSnS4 Nanocrystal Ink and Its Use for Solar Cells.* Journal of the American Chemical Society, (2009). **131**(33): p. 11672-11673.

[57]   Fouad, S.S., et al., *Multifunctional CZTS thin films: Structural, optoelectrical, electrical and photovoltaic properties.* Journal of Alloys and Compounds, (2018). **757**: p. 124-133.

[58]   Dong, Y., H. Wang, and G.S. Nolas, *Synthesis and thermoelectric properties of Cu excess Cu2ZnSnSe4.* physica status solidi (RRL) – Rapid Research Letters, (2014). **8**(1): p. 61-64.

[59]   Goyal, D. and P. Malar, *Dry mill route for synthesis of single phase bulk and e-beam growth of thin films of Cu2ZnSnSe4 for photovoltaic applications.* Journal of Alloys and Compounds, (2020). **846**: p. 156464.

[60]   Narica, P., et al., *Technology for Obtaining Cu2ZnSnSe4 Thin Films.* ENVIRONMENT. TECHNOLOGIES. RESOURCES. Proceedings of the International Scientific and Practical Conference; Vol 2 (2013): Environment. Technology. Resources. Proceedings of the 9th International Scientific and Practical Conference. Volume 2, (2015).

[61]   Tuan, D.A., et al., *A method to improve crystal quality of CZTSSe absorber layer.* Journal of Sol-Gel Science and Technology, (2018). **87**(1): p. 245-253.

[62]   Ashfaq, A., et al., *Tailoring the thermoelectric properties of sol-gel grown CZTS/ITO thin films by controlling the secondary phases.* Physica B: Condensed Matter, (2019). **558**: p. 86-90.

[63]   Sharma, S.D. and S. Neeleshwar, *Thermoelectric properties of hot pressed CZTS micro spheres synthesized by microwave method.* MRS Advances, (2018). **3**(24): p. 1373-1378.

[64]   Fahad Mehmood, et al., *Effect of annealing temperature on microstructure and thermoelectric transport properties of Cu2.1Zn0.9SnSe4 alloys.* Journal of Materials Science volume, (2021). **56**: p. pages20087–20097

[65]   Tripathi, S., B. Kumar, and D.K. Dwivedi, *Study on formation and characterization of kesterite CZTSSe thin films deposited by thermal evaporation technique for solar cell applications.* Journal of Materials Science: Materials in Electronics, 2020. **31**(11): p. 8308-8315.

[66]   I., S. and E.E.S.F.S. Belov N. . Paul Ewald, *50 Years of X-Ray Diffraction.* Springer., (1962): p. 351.

[67]   Patterson, A.L., *The Scherrer Formula for X-Ray Particle Size Determination.* Physical Review, (1939). **56**(10): p. 978-982.

[68]   Goldstein, J.I., et al., *Electron-Beam-Specimen Interactions*, in *Scanning Electron Microscopy and X-Ray Microanalysis: A Text for Biologist, Materials Scientist, and Geologists*, J.I. Goldstein, et al., Editors. (1981), Springer US: Boston, MA. p. 53-122.

[69]   al., M.D.e., *Von Ardenne and the scanning electron microscope.* Proc. Roy. Microsc. Soc, (1988). **23**: p. 283–288.

[70]   V, Z., H. J, and Snyder R., *A scanning electron microscope.* ASTM Bull, (1942). **117**: p. 2–15

[71]   Zheng, X., et al., *P-type quaternary chalcogenides of Cu2ZnSn (S, Se) 4 nanocrystals: Large-scale synthesis, bandgap engineering and their thermoelectric performances.* Journal of Alloys and Compounds, (2018). **738**: p. 484-490.